Department of Physics and Astronomy
Heidelberg University

Bachelor Thesis in Physics

submitted by

Hagen Tockhorn

born in Siegen (Germany)

2021

Improving the signal selection for trigger-level, low-mass resonance searches with ATLAS

This Bachelor Thesis has been carried out by Hagen Tockhorn

at the

Kirchhoff-Institute for Physics in Heidelberg

under the supervision of

apl. Prof. Dr. Monica Dunford

Improving the signal selection for trigger-level, low-mass resonance searches with ATLAS

The search for dijet resonances is a strong tool to investigate Physics beyond the Standard Model such as dark matter. If an unknown, massive particle is produced in a collision, it could decay into two Standard Model particles and leave a distinct signature in the invariant mass distribution of the two jets. Due to high production cross-sections as well as finite readout capacities, the search for sub-TeV dijet resonances at the LHC is statistically limited. The ATLAS trigger-level analysis covers this part of the spectrum by recording a strongly reduced set of event-level information processed by the High Level Trigger for all events passing the seeding Level-1 trigger. This has so far allowed for lowering the minimal detectable dijet resonance mass from ≈1 TeV to 450 GeV using the Level-1 triggers J75 and J100. To further lower this threshold, this thesis presents a signal selection strategy that selects the efficient phase space based on the dijet mass to optimize the selection criteria for TLA dijet searches. Additionally, the potential of including even lower p_T Level-1 triggers is investigated. The performed study is based on the analysis of proton-proton collisions at $\sqrt{s} = 13$ TeV at an integrated luminosity of 30.4 fb^{-1}, recorded by the ATLAS detector at the Large Hadron Collider in 2016.

Optimierung der Eventauswahl für eine Suche nach Trigger-Level Dijet Resonanzen am ATLAS Detektor

Die Suche nach Dijet-Resonanzen ermöglicht die Erforschung von physikalischen Phänomenen jenseits des Standardmodells (SM), wie zum Beispiel dunkler Materie. Falls ein neues, massereiches Wechselwirkungsteilchen in einer Teilchenkollision entsteht, könnte dieses in zwei Standard Model Teilchen zerfallen, was als Resonanz im invarianten Massenspektrum des Dijets beobachtet werden würde. Aufgrund eines hohen Wirkungsquerschnitts und limitierter Detektorkapazitäten, sind Suchen nach Dijet-Systemen mit Massen unter 1 TeV statistisch begrenzt. Die ATLAS Trigger-Level Analysis umgeht diese Restriktion indem nur begrenzte Eventinformationen verarbeitet werden. Mit der erhöhten Ausleserate können mit den Level-1 Triggern J100 und J75 somit Dijet-Resonanzen bis Massen von 450 GeV gesucht werden. Diese vorliegende Arbeit präsentiert eine neue Auswahlstrategie, mit der der effiziente Phasenraum bzgl. der invarianten Dijet-Masse ausgewählt wird. Unter diesem Grundsatz, werden die Event-Auswahlkriterien optimiert, sodass noch niedrigere Massen ausflösbar werden. Zudem wird das Potential von Level-1 Triggern mit niedrigeren Schwellenwerten analysiert. Die zugrundeliegenden Daten wurden 2016 in Proton-Proton Kollisionen bei $\sqrt{s} = 13$ TeV und einer integrierten Luminosität von 30.4 fb^{-1} mit dem ATLAS Detektor am LHC aufgenommen.

Contents

Chapter 1

Introduction

Since its first discovery in the 1930s, dark matter has been an enigma to the world of physics [1]. Despite the compelling amount of evidence that points towards its existence, no experimental signatures have yet been able to support the theories that aim to explain its nature.
The Standard Model of Particle Physics (SM) is one of the most successful theories in modern science. Its success is founded on a number of major theoretical predictions that were later experimentally confirmed [2–4]. Despite its great achievements, the Standard Model includes no viable particle candidate that is able to account for the observations made from dark matter [5]. However, this gives rise to numerous theoretical extensions beyond the SM that could explain the characteristics of dark matter.
In a simple theoretical model, dark matter is incapable of coupling directly to Standard Model particles, but rather performs interactions via a hypothetical particle mediator Z'. Given that Z' couples to both quarks and dark matter, it could be produced in a hadron collider [6].
The Large Hadron Collider (LHC) is the world's largest and highest energetic particle collider, enabling proton-proton collisions at unprecedented center-of-mass energies. If a Z' mediator is produced in a collision and decays back into two quarks, two collimated jets of hadrons (dijet) would form a characteristic resonance in the invariant mass distribution at the mediator mass. The search for such *dijet resonances* is not limited to dark matter but can further be applied to a variety of new physics beyond the Standard Model.
The ATLAS detector, located at the LHC, has been searching for such resonances at large mass values without any significant excess [7, 8]. Due to limitations on the transfer bandwidth, the detector is incapable of recording every occurring bunch crossing and needs to employ a sophisticated trigger system in order to select only events of interest. Since cross sections increase rapidly for lower-p_T interactions, low threshold triggers only record a fraction of the passed events to cope with the high particle production rates. In consequence, the detector sensitivity to dijet events with invariant masses in the sub-TeV range is considerably decreased.
To circumvent this statistical limitation on the search for light dijet resonances, the ATLAS Trigger-Object Level Analysis (TLA) is recording events with strongly reduced jet information. Bypassing the readout limitations, TLA is able to largely

restore the loss in statistics and probe for resonance masses down to 450 GeV [8]. These searches were conducted using the Level-1 (L1) single-jet triggers J75 and J100 that correspond to jet energy thresholds of 75 and 100 GeV.
This thesis presents a novel signal selection strategy that selects the efficient phase space based on the dijet mass. Under this keynote, the signal selection criteria of the aforementioned triggers will be optimized to probe for the presence of even lighter particle mediators. In addition, L1 single-jet triggers with lower trigger thresholds will be investigated under this event selection approach to examine their potential of further extending the sensitivity region to lower invariant masses.
The structure of this thesis is as follows. In Chapter 2, the Standard Model and, more specifically, Quantum Chromodynamics will be outlined, leading into a description of the formation of jets in proton-proton collisions. Further, the shortcomings of the Standard Model and searches for dark matter in particle colliders will be discussed. The experimental foundations are presented in Chapter 3 with special focus on the LHC as well as the ATLAS detector and its trigger system. The current status and the challenges of the search for light dijet resonances is reviewed in Chapter 4, followed by an overview of the TLA. Chapter 5 comprises an extended analysis on optimizing the signal selection parameters for a selection of Level-1 single-jet triggers.

Chapter 2

Theoretical Foundation

This thesis focuses on the signal selection of events with two-jet final states which are produced in proton-proton collisions at the Large Hadron Collider. In order to give an understanding of the underlying physical processes of dijet events, this chapter aims to summarize the theoretical background.
A general overview of the Standard Model and its constituents is given in Section 2.1, followed by a brief introduction to the theory of Quantum Chromodynamics in Section 2.2. Based on this foundation, Section 2.3 explains the formation of *jets* in proton-proton collisions with further reference to the kinematic variables. Finally, Section 2.4 covers theories beyond the Standard Model and gives an introduction to dark matter searches in particle colliders.

2.1 The Standard Model

The Standard Model (SM) of particle physics is a theory describing three of the four fundamental forces of the universe as well classifying its elementary particles. In this sense, it is one of the most extensive and profound theoretical models. However, lacking an explanation of the gravitational force, it does not give a full theory of the fundamental interactions.
Mathematically, the SM is classified as a gauge quantum field theory, describing interactions through quantum fields and the partaking elementary particles in terms of field quanta of their respective excitations. The gauge character of the Standard Model indicates that the Lagrangian, or its physical state, stays invariant under local transformations represented by certain Lie groups.
The aforementioned fields can be classified according to their internal angular momentum (spin), in units of $\hbar$, as spin-$\frac{1}{2}$ fermions (or "matter-fields"), spin-1 bosons (or "interaction fields") and the Higgs boson with spin 0. Figure 2.1 gives a schematic overview of the twelve fermions, five bosons as well as the three fundamental forces encompassed in the Standard Model.

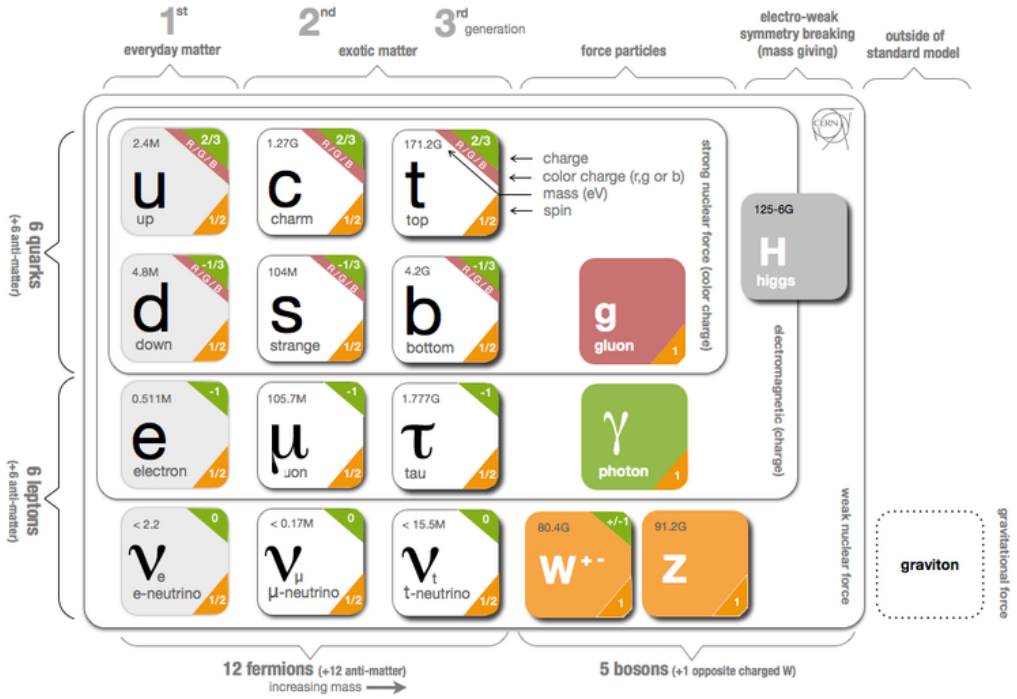

Figure 2.1: The elementary particles and force-carriers of the Standard Model, shown with some of their properties and schematically allocated to the respective interactions. Taken from [9].

Fermions

As mentioned above, fermions are spin-$\frac{1}{2}$ particles and therefore respect the Pauli exclusion principle according to the spin-statistics theorem [10]. The Standard Model describes a total of twelve fermions, further sub-classified into leptons and quarks. There are six leptons, all carrying a weak isospin and three additionally carrying an electric charge: the electron (e), muon (μ) and the tau (τ). These are heavy compared to their massless[1] neutrino counterparts ν_e, ν_μ and ν_τ.
In addition, there are six types of quarks: up (u), down (d), charm (c), strange (s), top (t), bottom (b). These are massive particles carrying fractional electrical charges. Up, charm and top quarks are also referred to as up- type quarks, sharing an electrical charge of $+\frac{2}{3}$. Likewise, the down, strange and bottom quarks are referred to as down-type quarks with an electrical charge of -$\frac{1}{3}$. All quarks carry a weak isospin as well as a color charge, the latter being further discussed in the following section.
All fermions have an anti-particle of same mass but opposite quantum numbers. Both quarks and leptons can be further split up into pairs referred to as *generations*. As for the quarks, these pairs consist of one up-type and one down-typ quark, whereas one charged lepton particle and its corresponding neutrino form

[1] In the current Standard Model of Particle Physics, neutrinos are defined as massless particles. However, numerous experiments suggest that neutrinos in fact possess a small mass based on the observations of neutrino oscillations [11, 12]. Since the underlying mechanism has not yet been fully understood, they are still referred to as massless in the SM.

a lepton-generation. Since the respective particles of each generation surpass the mass of its predecessor, the first generation is stable in the sense that its particles make up all ordinary (baryonic) matter. This would be represented by an up and down quark pair as well as an electron and ν_e pair.

Bosons

The Standard Model yields a description of three fundamental forces: the electromagnetic force (QED), the weak nuclear force and the strong nuclear force (QCD). Their action is interpreted as the exchange of gauge bosons, referred to as *force-mediating* particles, between two interacting particles. They carry an instrinsic angular momentum of 1.
The electromagnetic force is mediated by the massless photon (γ). The strong nuclear force is mediated by gluons (g), which are massless particles carrying an intrinsic color charge. Since both possess a vanishing mass, their mediation range is indefinite. The mediators of the weak nuclear force are the W^-, W^+ and Z^0. Opposed to the two preceding bosons, these are massive particles and therefore restricted in their mediation range according to Heisenberg's uncertainty principle [13]. Lastly, the Higgs boson, a massive spin-0 particle, gives a physical description why some elementary particles carry mass and others - photons and gluons - do not.

2.2 Quantum Chromodynamics

Quantum Chromodynamics (QCD) is the quantum field theory describing the strong nuclear force. Similar to the electromagnetic force requiring an electric charge, QCD only applies to quarks and gluons, also referred to as *partons*, since they carry a color charge. The charge can be labeled as red (r), green (g) or blue (b), whereas anti-quarks carry an anti-color ($\bar{\text{r}}$,$\bar{g}$,$\bar{b}$).
Given that both interacting particles and force-mediating bosons carry a color charge, strong interactions are fundamentally different from the electromagnetic or weak force. Since QCD shows an intrinsic invariance under local phase transformations of the *SU(3)* symmetry group, it is declared a non-abelian gauge theory. This enables gluons not only to interact with quarks but furthermore allows for gluon self-interactions.
For reasons not yet analytically proven, no observations of a single parton were made to date. In fact, quarks are naturally found in bound states referred to as hadrons. More specifically, systems of three quarks are named *baryons*, while *mesons* are composed of a quark and an anti-quark. The most well-known baryon is the proton, composited of two up and one down quark. It is furthermore the only stable baryon, where in contrast all mesons are inherently unstable. Bound states are a consequence of the fact that colored objects always seek color singlet states in order to propagate freely, implying a net of zero color charge. This phenomenon is referred to as *color confinement* and its origin is assumed to lie in the self-interacting character of the gluons.

A significant characteristic of QCD, which stands in stark contrast to color confinement, is posed by the concept referred to as *asymptotical freedom*. It describes the relation between the strong coupling constant α_s, which denotes the strength of force exerted in a strong interaction, and the momentum transfer Q between the interacting particles. Here, α_s is not constant but rather a function of Q - a peculiarity originating in the contribution of higher order Feynman diagrams. In low-Q regimes, α_s is of order $\mathcal{O}(1)$ but becomes asymptotically smaller for increasing transfer of momentum or decreasing length scales. Hence, partons can be approximated to quasi-free particles under these conditions.

2.3 Proton-Proton Collisions

2.3.1 Jet Formation

In accordance with color confinement, partons can not be detected as free particles. Instead, gluons and quarks leave an experimental signature in detectors in the form of a variety of color-neutral objects, collectively referred to as *jets*. These are collimated particle sprays, mainly constituted of hadrons but also leptons and photons. A brief description of the formation of jets in proton-proton collisions will be given in the following, with reference to descriptions given by [14, 15].

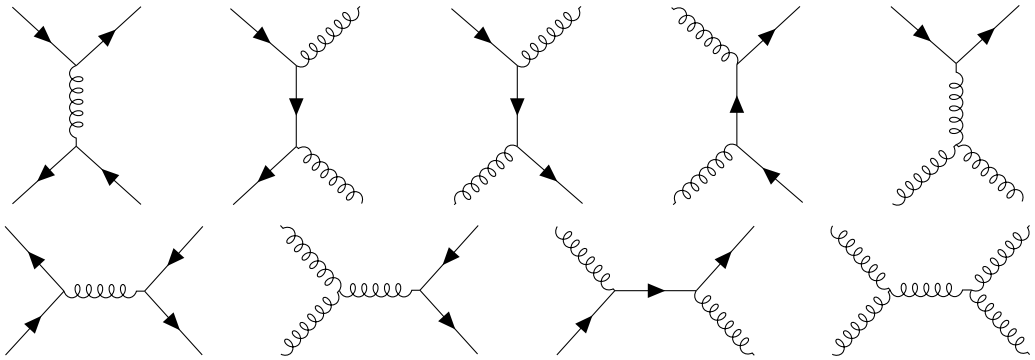

Figure 2.2: Selection of Feynman diagrams for sub-processes responsible for two-jet production in proton–proton collisions. Both $\hat{s}$ and $\hat{t}$-channel diagrams are shown in different combinations of initial- and final-state partons.

In the preceding section, protons were introduced as clusters of quarks and gluons bound together to form a color-neutral particle. Following this description, a proton can be thought of as a bag of *partons*, suggesting that a proton-proton collision is to be understood as an interaction between their constituents. When two high-energy partons collide, a high-Q interaction between them occurs, referred to as a *hard scattering process*. In a hard scattering process, mostly standard QCD processes occur such as those shown in Figure 2.2. Alternatively, a short-lived resonance particle could be created which might later decay back to two partons. The kinematics of each of the incoming partons is well-defined by a Parton Distribution Function (PDF) with respect to the momentum of its originating proton.

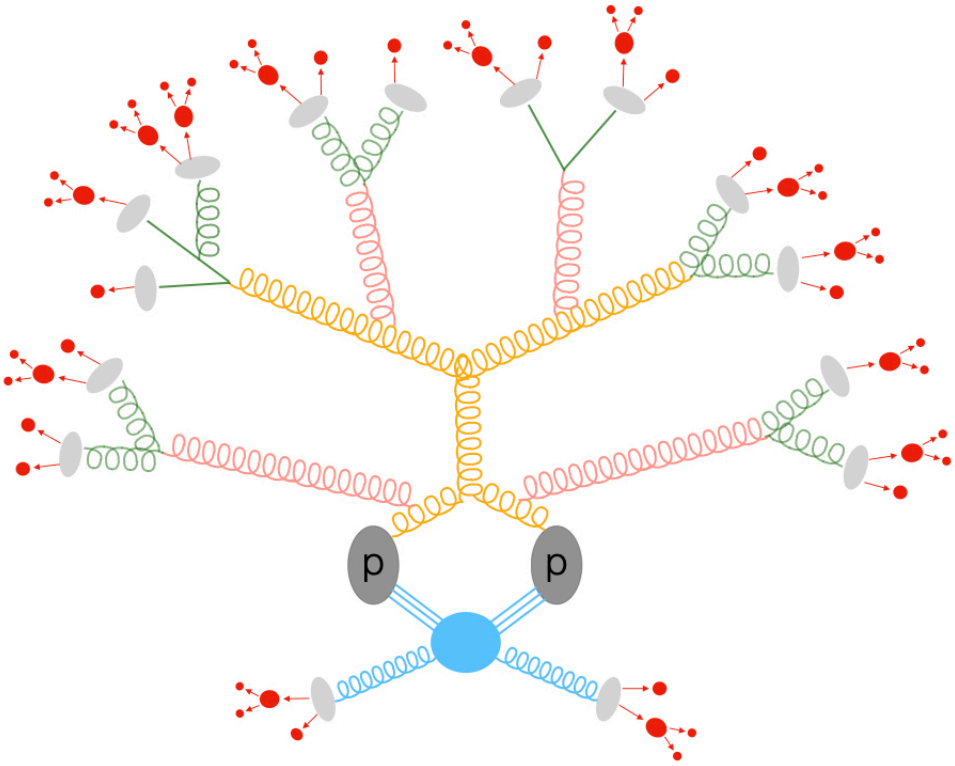

Figure 2.3: Illustration of the jet formation resulting from a proton-proton collision. The hard scattering process $gg \rightarrow gg$ is shown in yellow. The underlying event is depicted in blue color. Initial State Radiation (ISR) from the incoming partons and Final State Radiation (FSR) from the outgoing partons is shown in pink. Additional parton production is shown in green. The hadronization process is indicated by grey ellipsis and the resulting hadrons are shown in red. This figure is adapted from [15].

PDF's give the probability to find partons in a hadron as a function of the fraction x of the proton's momentum carried by the respective parton.
In addition to a hard scattering process, numerous other processes occur along a parton-parton collision, further contributing to the composition of the resulting jet. Accelerated incoming partons are likely to radiate particles such as photons or gluons, resulting in *Initial State Radiation* (ISR). The same holds true for the outgoing particles, forming the *Final State Radiation* (FSR). For sufficiently high energies, particles resulting from these interactions can split into additional partons emitted along the initial flight direction (e.g. $g \rightarrow gg$, $g \rightarrow q\bar{q}$). This results in a cascade of narrow-coned parton showers, propagating in the approximate direction of the original parton. Interactions of partons not involved in the hard-scattering process are collectively referred to as the *underlying event*.
Once the partons separate further after the collision and reach lower energies, the QCD coupling strength increases, making them no longer asymptotically free. At this point color confinement takes over, clustering the partons together in color singlet states, a process referred to as *hadronization*. Thus, each shower

of additionally produced partons now forms a collimated shower of hadrons in the direction of its initiator. This clustered group of hadrons is called a jet. A schematic illustration of the formation of jets from a $gg \rightarrow gg$ hard scattering process is given in Figure 2.3.

2.3.2 Hadron Collision Kinematics

This thesis focuses on events originating in hadron-hadron collisions. To allow for accurate physical descriptions, this section will give brief definitions of the underlying kinematics and associated variables following [16, 17]. Due to the particulate nature of hadrons, a collision is interpreted as an interaction between the respective partons of each hadron. The kinematics of such an event can be fully described by the fractions of momentum x_1, x_2 of the partons with respect to their originating hadron and the transfer of momentum Q.
At colliders like the LHC, collisions take place in the center-of-mass (COM) frame of the proton-proton-system which differs from the COM-frame of the colliding partons. Hence, in processes such as $pp \rightarrow 2$ jets + X, the final jets are boosted longitudinally relative to the lab frame. This is also referred to as the beam axis, conventionally defined as the z-axis of the lab-frame. As a result, high-energy experiments tend to use kinematic variables invariant under boosts along the beam axis, namely transverse momentum p_T, rapidity y and the azimuthal angle Φ.
The component of momentum in the plane transverse to the beam axis for a jet defined by the four-vector (E, p_x, p_y, p_z) is given by

$$p_T = \sqrt{p_x^2 + p_y^2}. \tag{2.1}$$

To fully describe the cross-section of the interaction, the jet angles relative to the beam axis are described by the rapidity

$$y = \frac{1}{2} \ln \left(\frac{E + p_z}{E - p_z} \right), \tag{2.2}$$

where E and p_z denote the jet energy and momentum along the beam axis.
The invariant mass of a jet, referred to as *jet mass*, is defined by the jet constituents and differs from the mass of the primary parton. In high-energy interactions, the jet mass is negligible compared to its energy, yielding the so-called pseudorapidity

$$\eta = -\ln \left(\tan \frac{\Theta}{2} \right), \tag{2.3}$$

an approximation of the rapidity y, where Θ denotes the polar angle.
Lastly, the relative angular separation between two particles in the (η, Φ)-plane is defined as

$$\Delta R = \sqrt{(\Delta\Phi)^2 + (\Delta\eta)^2}. \tag{2.4}$$

2.4 Beyond the Standard Model

Despite the grand success of the Standard Model in predicting and explaining a variety of fundamental processes and particles in the universe, it is an incomplete theory. This section aims at giving a brief overview of some of the most significant shortcomings of this theoretical framework.

The most considerable flaw of the Standard Model is its incompatibility with the theory of general relativity, hence lacking a description of the gravitational force. For energies below the Planck scale ($\sim 10^{16}$ TeV), gravitational interactions are significantly weaker than those of other forces and can therefore be neglected. However, approaching the Planck scale, the strength of gravity becomes comparable to the three remaining fundamental forces and effects of quantum gravity can no longer be neglected [18]. At this point, the Standard Model breaks down, leaving no further explanation for the interactions.
Another shortcoming of the SM is related to the mass of neutrinos. In the Standard Model these are postulated as massless particles such as photons. However, the discovery of neutrinos oscillating between lepton flavors indicates that they in fact posses a non-vanishing mass [11, 19], which has not yet been fully explained by the Standard Model.
A further key deficiency of the Standard Model is its lacking ability to give an explanation of dark matter, despite the compelling experimental evidence for its existence. To date, dark matter still remains an enigma to science and no direct experimental evidence has yet been found to support the theoretical explanations. The following section will give a brief summary of the existing evidence and modern approaches.
In 1933, Swiss astrophysicist Fritz Zwicky observed that the rotation curves of galaxies in the Coma cluster are not in alignment with predictions made by the Newtonian/Keplerian gravitation law [1]. Under the assumption that only luminous matter accounts for the total mass of these galaxies, he estimated the velocity dispersion of galaxies in Coma to be ~ 80 kms^{-1}. Surprisingly, he observed velocities two orders of magnitude larger than his calculation, indicating that the cluster must contain more mass than is observed. Zwicky termed this unseen non-luminous mass as *dunkle materie* (dark matter). Since then, numerous such observations were made, all supporting the hypothesis that the amounts of visible mass are not in alignment with the current state of the universe [20–22].
Dark matter constitutes a substantial contribution to the formation and stability of structures in the universe [23]. In modern approaches, it is defined in three families according to its typical velocity in the universe: hot, warm and cold. Candidates for hot (HDM) and warm (WDM) dark matter particles are predominantly posed by relativistic light neutrinos and sterile neutrinos, respectively [24]. While the latter still remains a valid candidate, observations from the cosmic microwave background (CMB) have shown that the mass of observed neutrinos alone can not account for the entirety of postulated dark matter [25] [26].
The current standard cosmological model, termed the ΛCDM, is based on the concept of cold dark matter (CDM) constituted of slow, non-relativistic particles.

Λ further denotes the non-vanishing cosmological constant in general relativity which represents dark energy. This model predicts that baryonic matter only accounts for 5% of the total energy-matter density in the universe, with dark matter further contributing 23% and dark energy 72% respectively.
Despite the overwhelming evidence pointing towards the existence of dark matter, the Standard Model yields no suitable candidate for its explanation, giving rise to further extensions of and theories beyond the Standard Model. These suggest that dark matter is most-likely particulate, massive, electrically neutral and interacts via the gravitational force [27]. A well-suited CDM candidate, satisfying these requirements, is termed the *Weakly Interacting Massive Particle* (WIMP). It can be shown that such particle with a mass in the GeV-TeV range and weak-scale couplings could be able to produce the dark matter abundance observed today [28].
As their weakly interacting nature indicates, these particles would be able to interact with Standard Model particles, allowing for their production in particle colliders such as the LHC. The next section aims to further expand this idea and give reasonable approaches towards the detection of dark matter.

2.4.1 Dark Matter Searches in Particle Colliders

The search for dark matter embodies one of the major research fields of modern particle collider experiments, e.g. the LHC. Under the assumption that dark matter (χ) couples to Standard Model particles via the weak nuclear force, these particles could be produced in SM particle collisions. However, if produced, they transverse the detector without considerably interacting with the baryonic detector instruments. Since this makes direct searches impossible, the ATLAS experiment follows two main strategies for indirect dark matter detection [29].

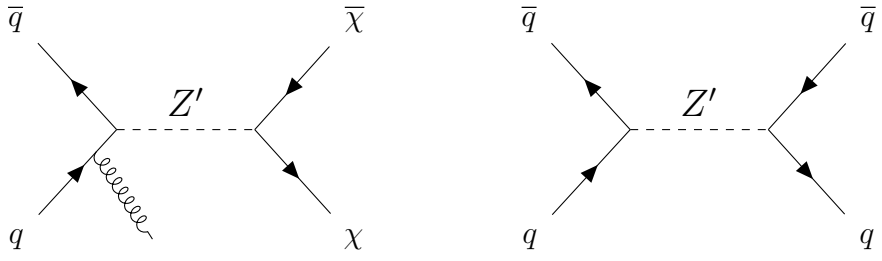

Figure 2.4: Feynman diagrams for weak interactions of an unknown mediator particle Z' coupling to dark matter and SM particles. Figure (a) depicts an interaction that is suitable for "Mono-X" search, whereas the interaction shown in (b) allows for detection of Z' via its dijet resonance.

In a simplified model, the coupling between dark matter and quarks is enabled through a weak scale mediator Z'. Since Z' couples to both quarks and dark matter particles, it can henceforth decay back into a particle-antiparticle-pair of

either sort. The first approach covers the case where Z' decays into a $\chi\bar{\chi}$-pair, outlined in Figure 2.4a. Since the produced particles can not be directly detected, an Initial State Radiation particle, e.g. gluon, could balance out the missing transverse energy E_T in the detector, leaving a characteristic signature in the detector. This is referred to as "Mono-X" search.
Alternatively, a decay of Z' into a $q\bar{q}$-pair, shown in Figure 2.4b, would result in a dijet-event as discussed in Section 2.3.1. Quantum Chromodynamics predicts a smoothly falling invariant mass distribution for dijet events, determined by the invariant mass of the two highest-momenta jets. Thus, jets originating from an s-channel production as in Figure 2.4b will form a localized resonance peak in the invariant mass spectrum at the mediator mass $m_{Z'}$. This detection strategy - however, not applied on dijet events - has proven to be successful before, allowing for the discovery of the Higgs Boson in 2012 [2].

Chapter 3

Experimental Foundation

The ATLAS detector is a large general-purpose particle detector located at the Large Hadron Collider (LHC) at CERN close to Geneva, Switzerland. Since its completion in 2008, the LHC has been colliding hadrons in pursuit of validating predictions of the Standard Model and searching for physics beyond it.
The Large Hadron Collider is introduced in Section 3.1, followed by a concise description of the ATLAS detector in Section 3.2. Lastly, the ATLAS trigger and data acquisition system is outlined in Section 3.3. More detailed descriptions of the LHC and ATLAS are provided in [30] and [31].

3.1 Large Hadron Collider

The LHC is the world's largest particle accelerator with a total circumference of 27 km located around 100 m underground. Accelerated high-energy protons collide at four different interaction points along the accelerator ring, where detectors are located (see Figure 3.1). These can be distinguished into general-purpose detectors - ATLAS and CMS - and more spezialized detectors - ALICE and LHCb. In terms of performance, particle colliders are typically characterized by their center-of-mass energy and luminosity. The center-of-mass energy $\sqrt{s}$ refers to the total energy available to the colliding particles in their respective center-of-mass frame. During its second data-taking period (2015-2018), the LHC reached an unprecedented center-of-mass energy of $\sqrt{s} = 13$ TeV. In order to attain such high energies, the protons are sequentially accelerated in a system of different accelerators as outlined in Figure 3.1. The pre-accelerated protons are injected into the main LHC ring in bunches of up to 10^{11} protons every 25 ns. There, the bunches are accelerated in opposite directions to their final velocities in two separate vacuum tubes and eventually lead to collisions in the respective detectors.
A second key characteristic of a particle collider is given by the instantaneous luminosity $\mathcal{L}_{inst}$ which poses a relationship between the cross-section σ of a physical process and its event rate in collisions $\frac{\partial N}{\partial t}$

$$\sigma \mathcal{L}_{inst} = \frac{\partial N}{\partial t}. \tag{3.1}$$

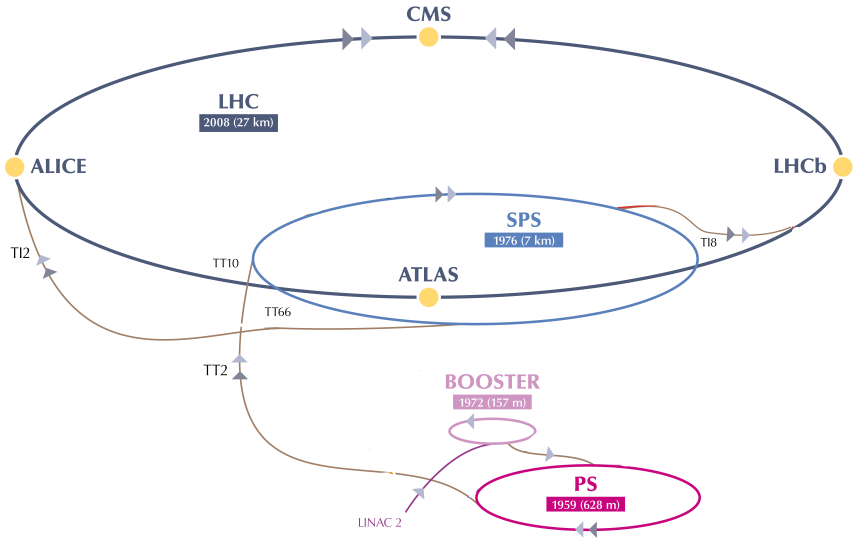

Figure 3.1: This figure shows a simplified schematic diagram of the LHC accelerator ring. The protons are pre-accelerated by various accelerators in the following order: a linear accelerator (LINAC), the Booster, the Proton-Synchrotron (PS) and the Super-Proton-Synchrotron (SPS). Afterwards, they are further accelerated in the LHC ring and lead to collisions in the detectors of ATLAS, ALICE, LHCb and CMS. This figure is adapted from [32].

In Particle Physics, the cross-section σ of an interaction is a measure for the quantum-mechanical probability of its occurrence. The quantity is given in units of barn, where 1 barn is equal to 10^{-24}cm^2. In this sense, processes with a low cross-section occur less frequently than those with a large cross-section.
By integrating the instantaneous luminosity with respect to time, one obtains the integrated luminosity $\mathcal{L}_{int}$ given by $\mathcal{L}_{int} = \frac{N}{\sigma}$. In order to search for rare events with a low cross-section, high luminosities are needed, emphasizing the importance of this quantity for the experiment. In peak performances, the LHC has reached luminosities of the order of 10^{34} $\text{cm}^{-2}\text{s}^{-1}$.

3.2 The ATLAS-Detector

The ATLAS-detector is a general-purpose detector with a cylindrically symmetric geometry. It measures 44 m in length, 25 m in diameter and accounts for over 7000 t in mass. The detector uses a right-handed coordinate system where the nominal interaction point determines the origin of the coordinate system and the positive z-direction coincides with the beam direction in anti-clockwise direction. Further, the positive y-direction points upwards and the positive x-direction towards the center of the LHC ring. Due to its geometry, measurements are generally expressed in cylindrical coordinates. The azimuthal angle Φ is measured around the beam axis, whereas the polar angle Θ defines the angle relative to the beam pipe [33].
The ATLAS detector reaches a maximum pseudorapidity of $|\eta| = 4.9$, limited by the beam pipe. In terms of detection instruments, ATLAS is constituted of

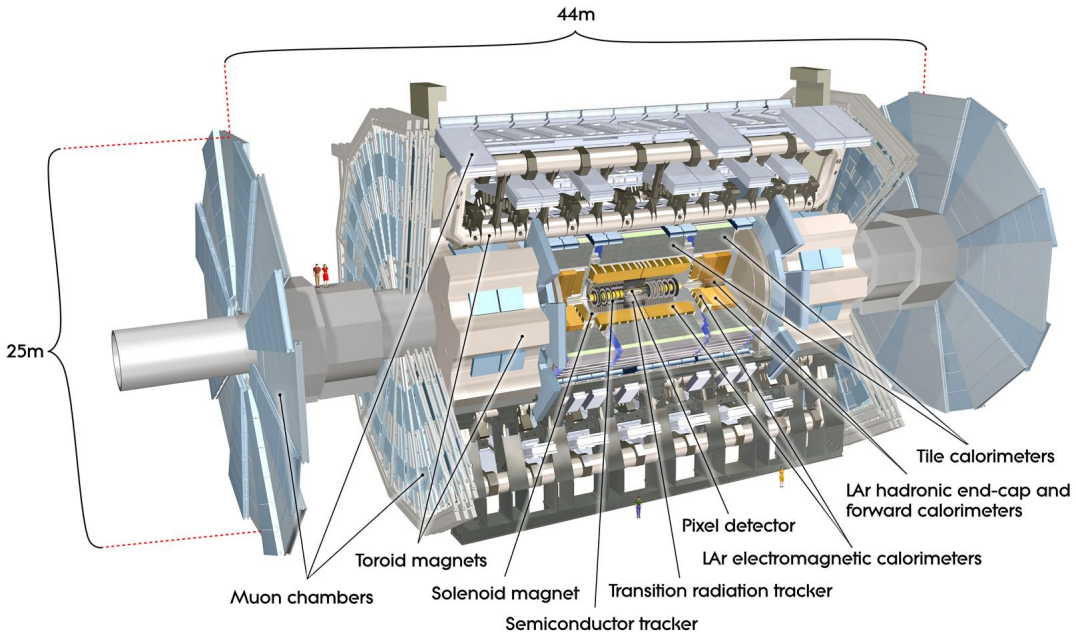

Figure 3.2: A schematic cross section of the ATLAS detector with emphasis on its concentrically arranged sub-detectors. This Figure was taken from [34].

different subdetectors concentrically wrapped around the beam axis. These are generally categorized into the inner detector, the calorimeter system and the muon spectrometer. A schematic cross section of the detector is given in Figure 3.2.

The Inner Detector

The inner detector comprises sub-detectors in close proximity to the interaction point of the collision. It is composed of a silicon pixel detector, silicon micro-strip detector and transition-radiation straw-tube tracker. The arrangement is further embedded into a 2T superconducting solenoid magnet. Hence, charged particles traversing the inner detector are bend in their trajectory by the induced Lorentz force. Combined with the fine granularity of the silicon sensors, this setup allows for precise measurements of particle trajectories from which their momenta and electric charges can be reconstructed. The inner detector is capable for particle tracking up to a pseudorapidity of $|\eta| = 2.5$ [35].

Calorimeters

The calorimeter system surrounds the inner detector. Its main purpose is to measure the energy of the particles produced in proton-proton collisions via different sampling techniques. The calorimeters are composed of alternating layers of active material, i.e liquid argon, and passive material, typically lead or steel. In contrast to the tracker systems of the inner detector, high-Z materials are chosen for the calorimeters. This provokes that incident particles loose their energy

through interactions with the passive material (absorber) and set off a cascade of secondary particles referred to as *shower*. Subsequently, a signal is induced in the neighboring active material via ionization or scintillation. Since this reflects the energy of the shower particles, the total energy of the incident particle can be reconstructed from such measurement.
In the GeV range, electrons, positrons and photons mainly loose energy in the absorber material due to bremsstrahlung and pair-production, resulting in an electromagnetic shower of secondary particles. As the cascade develops, the particles eventually take on energies in the MeV range where the photoelectric effect and ionization dominate the energy loss and allow for detection in the *electromagnetic calorimeter* (ECal).
Hadronic particles, i.e protons or pions, typically engage in inelastic nuclear interactions with the absorber material, making the resulting hadronic shower significantly more complex than the electromagnetic counterpart. As a consequence, the *hadronic calorimeter* (HCal) possesses a more complex structure than the ECal to ensure good $|\eta|$-coverage and precise jet reconstruction. Generally, the calorimeter system is able to detect the majority of incident particles, with the exception of muons and neutrinos.

Muon Spectrometer

Due to their relatively high invariant mass, muons naturally do not deposit much energy in the calorimeters. The outermost detector system of ATLAS consists of around 1,150 muon drift tube chambers (MDT) encapsulating a total of 350,000 individual drift tubes [36]. Embedded in a 2.8T toroidal magnet, this setup allows for precise muon identification and momentum measurement.

3.3 The ATLAS Trigger System

During Run 2 of the LHC, a bunch-crossing rate of 40 MHz was recorded. Since a fully recorded event is processed in the order of seconds and bandwidth as well as storage capacity are limited quantities, the ATLAS detector is incapable of processing every single bunch-crossing event. Therefore, a reliable Trigger and Data Acquisition System (TDAQ) is an essential component of the ATLAS detector to ensure a sufficient event rate reduction.
The trigger system of ATLAS consists of two independent levels, a hardware-based *first level* (L1) *trigger* and a software-based *high level trigger* (HLT). This system is optimized to decide whether an event is discarded or passed to the data acquisition system (DAQ) where the event data is stored for future reconstruction and analysis. The underlying trigger selection criteria are based on a set of predefined conditions termed *trigger items* which are stored in the trigger menu [37]. The trigger decisions are taken with regard to indicators such as missing transverse energy or jets and other object multiplicities such as photons, electrons or muons exceeding the kinematic thresholds. In general, objects that are being reconstructed in parallel to the run - *online* - are referred to as trigger objects,

whereas those reconstructed from stored data points are termed *offline* objects. In this sense, reconstruction denotes the transformation of raw detector information into objects which can be identified as particles.
The high instantaneous luminosity of the LHC creates a high density hadronic environment in the detector, leading to high detector occupancies. As a result, high trigger rates and a high rate of background processes from hadronic collisions, referred to as *pile-up*, make triggering a difficult task. To ensure full trigger efficiency and a high signal purity under these conditions, the TDAQ system encompasses a rather complex system, as outlined in Figure 3.3.

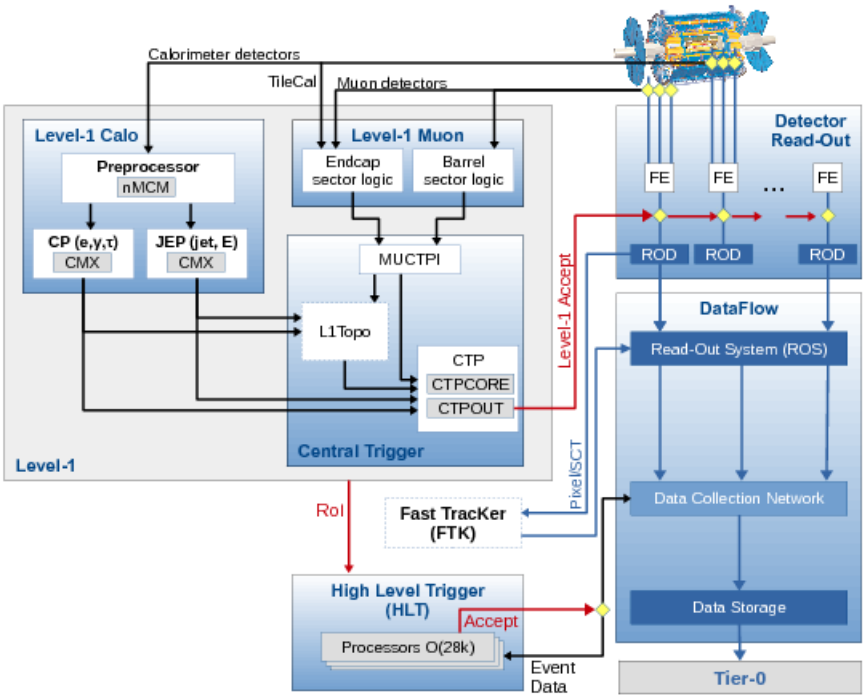

Figure 3.3: An overview of the ATLAS Trigger and Data Acquisition System. This figure is taken from [38].

3.3.1 The Trigger Menu

The trigger menu is responsible for the administration of the various trigger systems and their respective decision conditions. The stored trigger items define these conditons based on e.g. kinematic thresholds or particular particle contents, motivated by the experimental objectives and interests. The trigger menu further comprises a list of full L1 to HLT trigger selections, referred to as *trigger chains* [37]. Generally, trigger chains are a combination of Level-1 and HLT trigger objects. An example of a trigger chain would be HLT_4j45_L1_3J15. This defines a trigger system that requires events in which at least three L1-jets with transverse energy above 15 GeV were identified and at least four jets with transverse energies above 45 GeV were identified by the HLT for the same event.

In this example, the L1_3J15 trigger element represents the so-called *seed* for the HLT_4j45 trigger element, since the latter only evaluates a decision after the event has already passed the requirements of the L1 trigger item [39].
To further reduce the trigger chain rate, a prescaling factor can be applied to each stage of the chain. A prescaling factor of n indicates that only one out of n events which satisfies the trigger requirements is kept. These individual constraints on the trigger chain enable maximum use of the available bandwidth for luminosity fluctuations, making the trigger menu a dynamical system [37].

3.3.2 The Level-1 Trigger

The main task of the L1 trigger system is to reduce the initial collision rate of 40 MHz to 100 kHz for the readout. The decision time per bunch-crossing is less than 2.5 μs. To adhere to this constraint, L1 uses information with reduced granularity from the calorimeters and the muon detector. Objects that are reconstructed online by the L1 trigger are collectively referred to as *L1 trigger objects*.
The Level-1 trigger system is composed of four sub-systems. The Level-1 Muon Trigger (L1Muon) and the Level-1 Calorimeter Trigger (L1Calo) process data at reduced resolution from their respective detectors for online trigger object reconstruction. This data is passed on to the Level-1 Topological Trigger System (L1Topo) and used to calculate kinematic quantities of each event, e.g. angular separation or invariant mass. With these quantities, L1Topo performs real-time event selection based on the kinematic and geometric relationships between the trigger objects [33, 40]. Eventually, multiplicities exceeding the kinematic and topological thresholds of the subsystems are passed on to the Central Trigger Processor (CTP). There the trigger objects are compared to the requirements specified in the trigger items. If these are fulfilled, a L1 Accept (L1A) signal is issued and the trigger item is passed to the HLT together with its Region-of-Interest (RoI). The RoI contains geographical coordinates (η,Φ) of detector regions with interesting event features.

3.3.3 The HLT Trigger

The HLT trigger system processes all events flagged with an L1A, causing a further event rate reduction to 1kHz. The online reconstruction of the HLT system is very similar to the one applied offline to data stored in the data streams. For every event passed to the HLT, the associated RoI is used as a seed for more advanced reconstruction algorithms taking advantage of full calorimeter granularity as well as additional information from the muon chambers and tracker detectors. At this point, the trigger chains are subject to a decision time of 200 ms, provoking that most algorithms only take the RoI into consideration for optimized computation time. If at least one trigger chain is passed, the event is stored in different data streams for offline reconstruction and analysis.

Chapter 4

Search for Light Dijet Resonances

In order to test and guide hypotheses that reach beyond the Standard Model, searches can be conducted on a variety of different final states and experimental signatures. This thesis will be confined on the search for resonances in dijet final states and henceforth explanations and interpretations will be given with reference to such events. In Section 2.4.1, a simplified model was introduced, where a hypothetical mediator particle Z' couples to both quarks and dark matter. Since it can be produced by the annihilation of both quark and dark matter particle-anti-particle pairs, it can henceforth decay back into either sort. As described in Section 2.3.1, a decay back into quarks would result in a dijet event, leaving a resonance or *dijet signature* in the invariant mass distribution of the respective dijet.

In the past, numerous experiments have searched for such dijet final states at different center-of-mass energies and with different data set sizes. Unfortunately, none was able to gather significant evidence for a possible new resonance. However, this should not discourage experiments from continuing to search for dijet resonances. As the center-of-mass energy of modern colliders increases, higher dijet masses become accessible. Further, an increase of luminosity allows for larger datasets and therefore increases the sensitivity to dijet final states with a low cross-section. The impact of these key factors on the sensitivity for dijet resonances is reflected in the exclusion limits on the quark coupling constant set by the research groups. An exclusion limit defines a contour above which couplings - here the coupling of quarks to the Z' boson - are excluded at a confidence level of 95%. Figure 4.1 shows the exclusion limits set by ATLAS in the plane of quark coupling g_q as a function of the mediator mass $m_{Z'_A}$ for an axial-vector model. It demonstrates that different invariant mass regions are accessible with the studied final-state signatures, allowing to probe for resonance masses as low as 100 GeV. Nonetheless, it is noteworthy that, except for the Dijet TLA search, all other searches have been relying on limited event statistics due to reduced readout rates. This emphasizes the necessity to continue searching for low resonance masses in dijet final states. At lower masses, especially below 400 GeV, exclusion limits are weaker and set by reduced datasets.

The reason for this is that as experiments achieve higher center-of-mass energies, they encounter an increasing amount of QCD background processes at lower

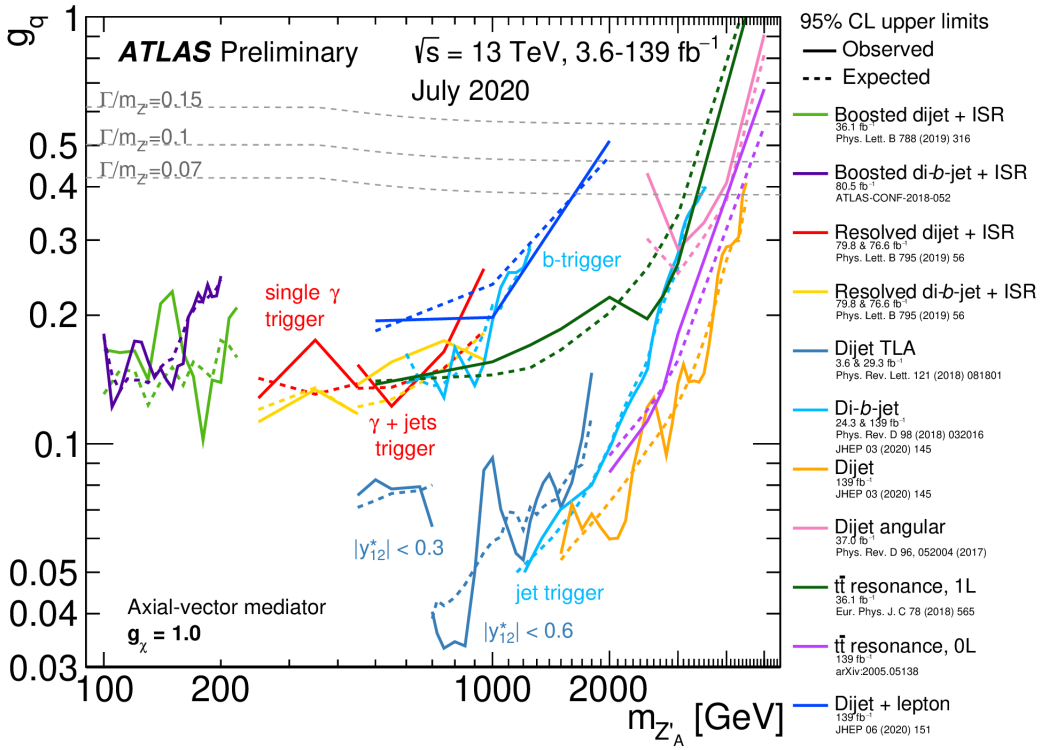

Figure 4.1: The exclusion limits for the quark coupling constant g_q as a function of the axial-vector mediator mass $m_{Z'_A}$. The limit contours are shown for a variety of final-state signatures at different center-of-mass energies and dataset sizes. The expected limits from each search are indicated by dotted lines. Taken from [41].

masses. In order to cope with these large background rates in the search for light dijet resonances, the ATLAS trigger-object level analysis (TLA) records only partial event information to circumvent the statistical limitations set by the ATLAS detector. The following section will give an introduction to this novel trigger and data analysis strategy.

4.1 Trigger-Object Level Analysis

The readout performance of the ATLAS detector is mainly limited by offline storage capacity, CPU processing time and transfer bandwidth. Thus, a complex trigger system is responsible to select only a fraction of all events for offline analysis. This selection process is based on the presence of high-p_T physics objects such as muons, electrons, photons, jets and missing transverse momentum [42]. Events that do not pass the trigger requirements are discarded. Therefore, the trigger system is ultimately responsible for the data that is available to the experiment. Events originating in QCD processes are the most frequent, provoking that high trigger thresholds need to be applied to physics events containing jets. Given that the jet production cross-section is significantly higher for low-p_T events compared to those with higher transverse momenta, single-jet triggers with low p_T

thresholds are prescaled in order to cope with the limitations of the detector. Prescaling refers to a procedure where out of all events only the inverse fraction of the prescale factor is kept for offline storage. Physics objects produced in low cross-section events, such as electrons or muons, are mostly unaffected by these selection constraints even for low transverse momenta. However, this does not apply to final states containing jets, where event rates are high and grow rapidly with the number of simultaneous proton–proton interactions, also referred to as *pile-up interactions* [43].
As a result, a large fraction of low p_T jets are discarded. Since the momenta of the two most energetic jets of the event and the invariant dijet mass are linearly correlated[1], searches for low dijet resonance masses are henceforth statistically limited. Figure 4.2 demonstrates that the application of prescales on low-p_T triggers reduces the statistics for sub-TeV invariant dijet masses by several orders of magnitude.

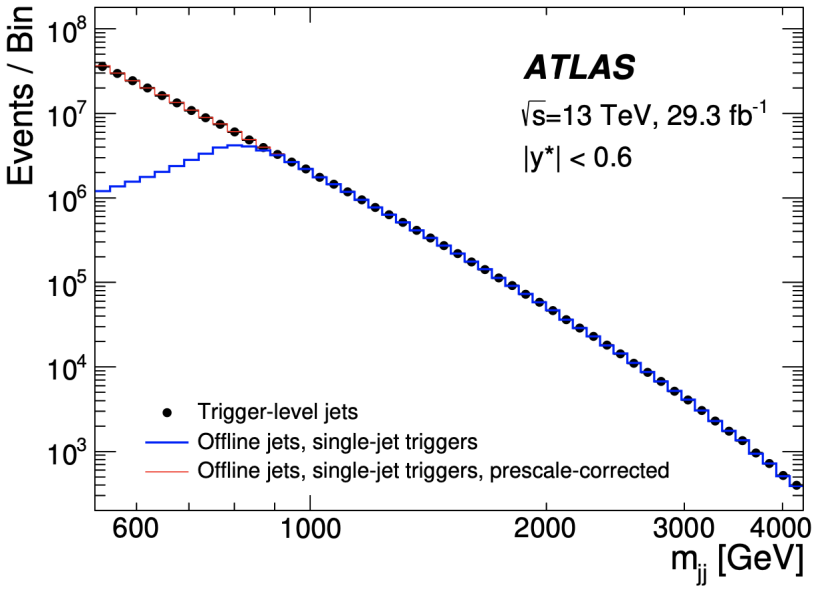

Figure 4.2: The invariant mass distribution for dijet final states considering different readouts. The events which pass the single-jet triggers are shown in blue, those which are further corrected for their prescale are shown in red and dijet events using trigger-level jets are depicted in black. Taken from [8].

The *Trigger-Object Level Analysis* poses a novel strategy to circumvent this statistical limitation. In their approach, only physics objects which were reconstructed in real-time within the HLT system are stored for later analysis. Thus, additional event information from the inner detector, muon spectrometer or the calorimeters are ignored for the object reconstruction. Such *trigger-level objects* are stored

[1]The invariant mass of a particle decay (e.g. gluon or Z' mediator) into two jets is given by $m_{12}^2 = (E_1 + E_2)^2 - \|\mathbf{p}_1 + \mathbf{p}_2\|^2$ where the indices refer to the most and second-most energetic jet.

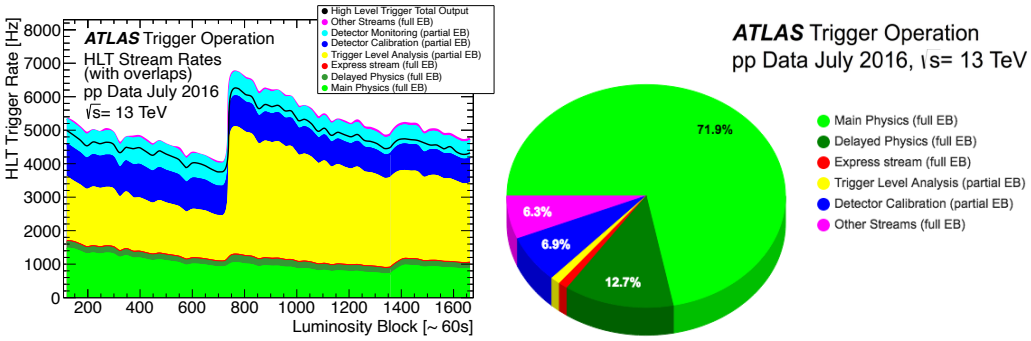

(a) (b)

Figure 4.3: The underlying data stems from a fill taken in July 2016 at a peak luminosity of $L = 1.02 \cdot 10^{34} cm^{-2} s^{-1}$. (a) Total and individual stream rates at the HLT as a function of the number of luminosity blocks which correspond to on average 60s per luminosity block. TLA stream rates are shown in yellow compared to Main Physics stream rates in green. An average pile up of $\mu = 24.2$ is given. (b) Contribution of the total output bandwidth of the various streams at the High Level Trigger for a peak pile up of $\mu = 35$. Both are taken from [45].

with only partial event information, effectively reducing the event size by 95.5% relative to a fully offline-reconstructed event [42].
From the definition of the bandwidth [44]

$$\text{bandwidth} = \text{event rate} \times \text{event size},$$

it becomes clear that a reduced event size allows for higher event rates at a fixed bandwidth. The algorithms responsible for online trigger object reconstruction at HLT level closely resemble the offline reconstruction [8] and are optimized to not contribute significantly to the overall trigger computing resources. In consequence, the TLA takes advantage of significantly higher HLT trigger rates relative to the Main Physics HLT rate while maintaining a minimal impact on the total bandwidth (see Figures 4.3a and 4.3b). As a result of these efforts, the TLA is able to largely restore the loss in statistics at and significantly increase the sensitivity to lower dijet resonance masses.

Event information are stored in a dedicated TLA data stream, called *Datascouting Stream* (DS). As far as jets are concerned, only the jet four-momentum as well as a set of variables needed for the jet identification and calibration are stored in the DS [42]. Jets recorded by the TLA are referred to as *trigger-level jets*, whereas *offline jets* are reconstructed with full event information and stored in the main physics stream. Both trigger-level and offline jet objects are reconstructed using the anti-kT jet reconstruction algorithm, which clusters contiguous calorimeter energy deposits (topological clusters) together into a jet with a radius parameter of $\Delta R = 0.4$ [46]. After storage, the jets are calibrated in a procedure that is very similar to the offline calibration [8]. In general, calibration of the stored objects is necessary to correct for known detector effects on physical quantities of trigger objects, e.g. transverse energy [15].

Chapter 5

Optimization of Signal Selection

Due to the reduced readout rate of the ATLAS detector for low-p_T single-jet triggers, the search for low dijet resonance masses is statistically limited. By recording strongly reduced event information, the ATLAS trigger level analysis was able to circumvent this limitation and effectively lower the minimal detectable resonance mass from roughly 1 TeV to 450 GeV [8].
An optimal signal selection aims to minimize the amount of recorded pile-up interactions to yield the best possible signal-to-background ratio for dijet resonances. Further, the selection criteria need to be chosen such that the events are selected at full trigger efficiency. Considering that the low invariant dijet mass (m_{jj}) regime is still of great relevance to probe for the presence of new particles, this thesis prioritizes the search for selection criteria which increase our sensitivity to lower invariant masses.
In this chapter, a novel approach towards signal selection will be presented which allows for the detection of dijet events with significantly lower invariant masses relative to the current selection approach of the TLA. The following analysis will study the implications and behaviour of this approach among additionally applied offline criteria in order to yield the best-possible selection criteria for light dijet resonances. Further, the potential of including even lower p_T Level-1 triggers is investigated in this context.
In Section 5.1, the general selection criteria for the considered events are outlined. Section 5.2 illustrates the effects of p_T, m_{jj} and $|y^*|$ cuts with special emphasis on the relation between the quantities. Afterwards, an introduction to trigger efficiencies will be given in Section 5.3. With these definitions clarified, Section 5.4 aims to give an overview of the current signal selection approach implemented by the TLA. In comparison, Section 5.5 will present a signal selection approach based on m_{jj} thresholds and analyse the implications of this.

5.1 Event Selection

For this analysis, data collected in 2016 is used, which was taken during LHC Run 2 at a center-of-mass energy of 13 TeV and luminosity of 30.4 fb^{-1}. All events are required to contain at least two trigger-level jets in a pseudorapidity range of $|\eta| <$

2.8. This ensures that we are not considering data taken from the forward region of the ATLAS detector where the jet energy resolution increases [33]. The jet objects were reconstructed at HLT-level, using only information from the ATLAS calorimeters. In a dijet event, the jet with the highest transverse momentum is termed the *leading* jet whereas the *subleading* jet refers to the jet with the second highest transverse momentum. Both jets are required to have $p_T > 85$ GeV in order to mitigate the impact of pile-up interactions on our data.
Further, considered dijet events are required to be below a $|y^*|$-threshold, where typical values are 0.3 and 0.6. This helps to reduce the background from QCD processes and take influence on the trigger efficiencies.

5.2 Preliminary Considerations

Given that this thesis aims at optimizing the selection criteria for dijet events, it is necessary to demonstrate the relations between the considered selection variables so that they can be considered in the following analysis. These are explicitly the leading and subleading jet p_T, the invariant mass as well as the $|y^*|$ requirement for trigger-level jets.
In an ideal dijet system, the leading and subleading jet p_T are balanced. However, additional jet activities lead to a slight asymmetry between both quantities, even though they are still strongly correlated. This indicates that the placement of leading jet p_T cuts on the event selection of the trigger affects the subleading jet p_T-distribution of the selected dijet systems. Since the invariant mass is reconstructed from the measured jet momenta, the p_T distributions of both jets likewise affect the m_{jj} distribution. This is demonstrated in Figure 5.1 which depicts the m_{jj} distribution against the subleading jet p_T distribution for different leading jet p_T cuts.

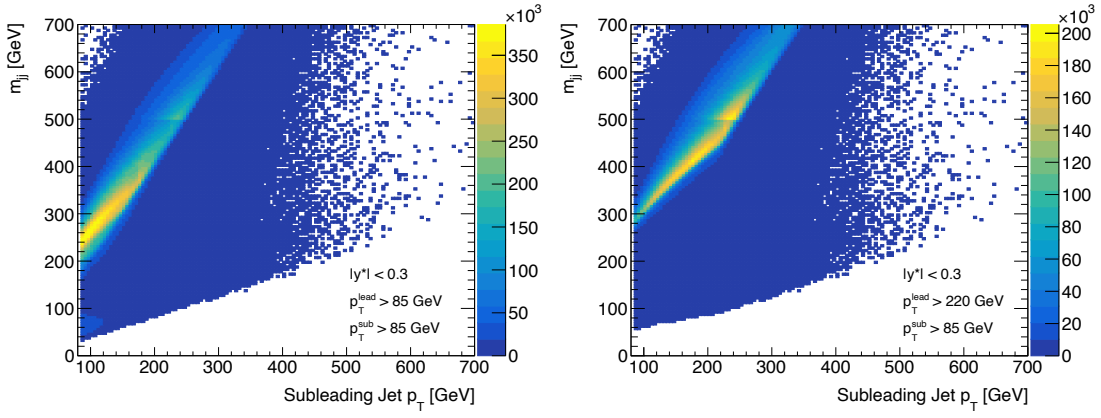

(a) $p_T^{lead} > 85$ GeV (b) $p_T^{lead} > 220$ GeV

Figure 5.1: The invariant mass of a dijet system against the subleading jet p_T for different leading jet p_T cuts. The results are shown for $|y^*| < 0.3$ and $p_T^{sublead} > 85$ Gev.

From Figure 5.1 it becomes clear that the invariant dijet mass and the subleading jet p_T show strong linear correlation, as indicated by the yellow band. Further, it can be observed that higher cuts on the leading jet p_T shift the distribution of the subleading jet p_T to higher values. This provokes that dijet events with lower invariant masses are discarded, shifting the distribution to higher m_{jj} values.
As mentioned in Section 5.1, a $|y^*|$-cut was introduced to constructively shift the trigger efficiency distribution to higher or lower invariant masses. The impact of this requirement is illustrated in Figure 5.2 which depicts the distribution of m_{jj} versus subleading jet p_T for $|y^*| < 0.3$ and no $|y^*|$ cut.

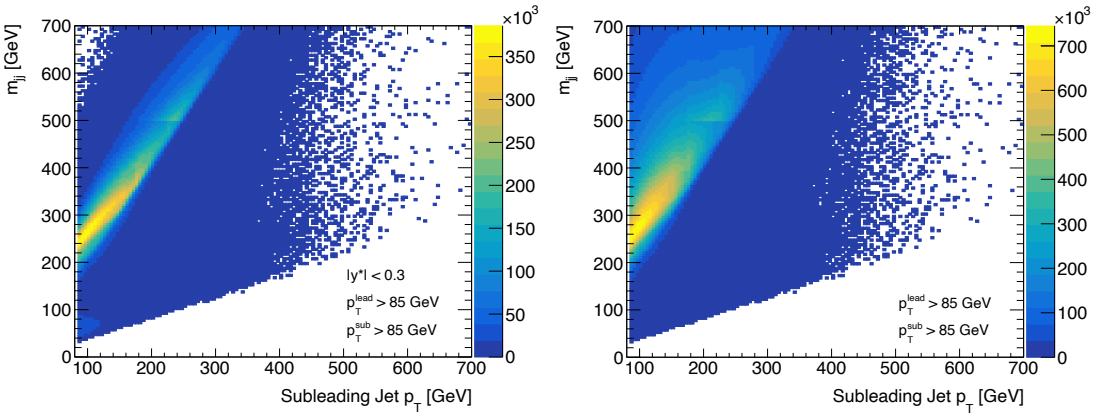

(a) $|y^*| < 0.3$ (b) no $|y^*|$ cut

Figure 5.2: The invariant mass of a dijet system against the subleading jet p_T for different $|y^*|$ cuts. The results are shown for p_T^{lead},$p_T^{sublead} > 85$ GeV.

Figure 5.2a reveals that placing a stringent $|y^*|$ cut on the event selection provokes that higher-p_T jets are selected for a given invariant mass, thus reducing the asymmetry between the leading and subleading jet p_T. In consequence, subleading jets are more likely to satisfy the event selection criteria, an implication that will be further discussed in Section 5.5. The following analysis presented in Section 5.5 takes these correlations of event kinematics and selection criteria into account to optimize the selection parameters.

5.3 Trigger Efficiency

As mentioned before, an optimal signal selection ensures that all triggers are running at full efficiency, which can be considered when the trigger exceeds an efficiency of 99.9%.
The Level-1 trigger system is responsible for selecting events to be stored in the Datascouting Stream of TLA. Thus, this thesis aims at optimizing the signal selection criteria of the following L1 single-jet triggers: J100, J75, J50 and J40. The nomenclature can be interpreted such that in example the L1 J100 trigger requires an event to contain at least one jet with a transverse energy exceeding the trigger threshold of 100 GeV to be passed on by the L1 trigger system. Due

to the high bunch-crossing rate of 40 MHz of the LHC, L1 is taking decisions at a rapid rate and with information of coarse granularity. Hence, the resolution of transverse energy at the L1 trigger system is significantly wider compared to the trigger-level jets at HLT [43]. Furthermore, L1 jets are only calibrated to the electromagnetic scale of the calorimeters, which means that a large fraction of the energy of the hadronic shower is invisible to the trigger [47]. As a result, the transverse momenta where the L1 triggers turn fully efficient are much higher than their nominal thresholds.
The point at which a trigger turns fully efficient is typically determined with the respective turn-on curve and will be further referred to as *turn-on point*. Figure 5.3 shows the trigger efficiency as a function of transverse momentum for the considered L1 triggers. The efficiency of a trigger is defined as the number of events

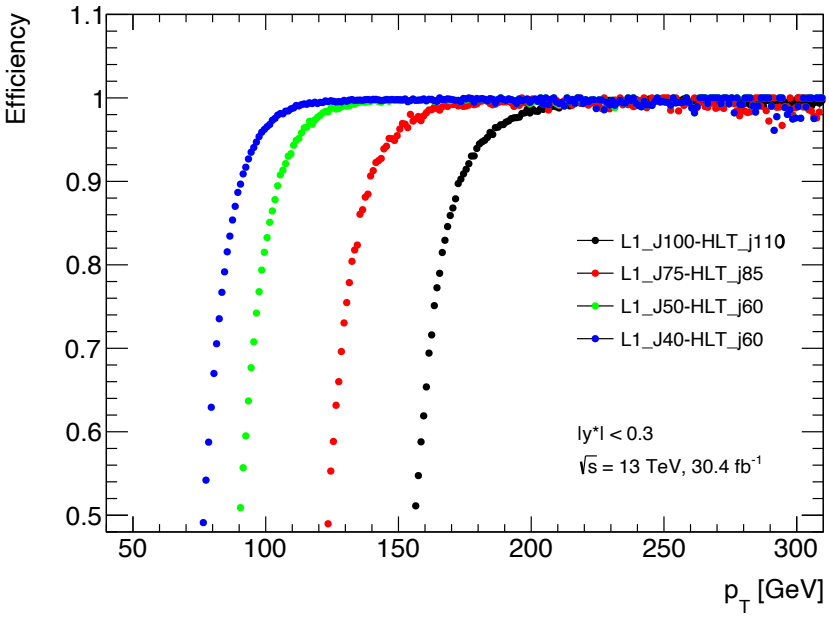

Figure 5.3: The turn-on curves of the L1 single-jet triggers J100, J75, J50 and J40. The efficiency is shown as a function of invariant dijet mass p_T.

that have passed the particular trigger relative to the total number of events. Since the absolute number of events can not be determined without a trigger, an HLT trigger-chain serves as a reference frame. To give an example, "L1_J100-HLT_j110" defines the efficiency of L1 J100 as the number of events that have passed both the L1 trigger and HLT trigger chain divided by the number of events which have passed the latter.
To determine the p_T threshold where the trigger turns fully efficient, a two-parametric sigmoid function is used as an ansatz to fit the curves,

$$\sigma(x) = \frac{1}{1 + e^{-a(x-b)}}. \tag{5.1}$$

The function is only fitted to efficiencies of 95% and above, since we are only interested in efficiencies close to 100%. With such fit, the transverse momentum

where the trigger exceeds an efficiency of 99.9% can be determined.
In order to avoid bias from the fitting technique, a thorough error calculation needs to be carried out. The statistical uncertainty from error propagation of the fit parameters can be determined with equation (5.2),

$$\Delta x = \sqrt{\left(\log\left(\frac{1}{y}-1\right)\left(\frac{\Delta a}{a^2}\right)\right)^2 + \Delta b^2}. \tag{5.2}$$

In this analysis, all statistical errors originating in fit uncertainties were of order $\mathcal{O}(0.1)$ GeV and are henceforth smaller than the chosen bin size of 1 GeV. To avoid bias from the fit range, the lower fit boundary was varied in steps of 1% between 80% and 95% efficiency. For each fit interval, the turn-on point was determined and the overall standard deviation with respect to the initial turn-on point was taken as a second statistical uncertainty. Since the choice of upper boundary showed no significant bias on the thresholds, this was not further taken into account. The yielded uncertainties were of order $\mathcal{O}(1)$ GeV, and will be further considered as the significant statistical error for the following analyses.

5.4 Preliminary L1 Trigger Selection Strategy

To motivate the study of new signal selection approaches, this section aims to give a brief overview of the currently implemented event selection strategy of the TLA and demonstrate the implications on the search for low resonance masses. This description is based on the outline given in [8].
In the current strategy, events must contain at least two trigger-level jets with $|\eta| < 2.8$. Given that the trigger decisions are carried out by the L1 single-jet triggers J100 and J75, jets are required to have either $E_T > 100$ GeV or $E_T > 75$ GeV, respectively. Upon these constraints, the subleading jet has to satisfy $p_T > 85$ GeV, whereas the leading jet is required to have $p_T > 185$ GeV or $p_T > 220$ GeV in order to fire the J75 or J100, respectively. The leading p_T cut is placed to ensure that events are selected at full trigger efficiency. This further implies that the leading jet has to fire the L1 trigger for the event to be recorded. For an event to pass the Level-1 J100, the two-jet final state is required to have $|y^*| < 0.6$, whereas the L1 J75 requires $|y^*| < 0.3$. The more stringent choice provokes that higher-p_T jets are selected at a given invariant mass, providing an increased sensitivity for lower invariant masses at fixed p_T cuts. These selection criteria allow the TLA to probe for resonance masses above 531 GeV with the L1 J100, whereas the J75 further extends the sensitivity region to invariant masses above 400 GeV.
Compared to traditional dijet searches at the LHC which were limited to invariant masses above 900 GeV [8], this poses a significant increase of sensitivity to lower mass regions. However, with regard to Figure 4.1, searches below 400 GeV might still yield interesting results since exclusion limits in these mass regimes are weaker and rely on reduced event statistics.
The limitation of the current signal selection towards lower masses originates in

the leading jet p_T constraints. Given that the leading jet is explicitly required to fire the L1 trigger, events with leading jets below the threshold are discarded. Due to the linear relationship between jet p_T and invariant mass outlined in Section 5.2, dijet events that fired the Level-1 J75 are only considered if they exceed 400 GeV in invariant mass. As mentioned above, the requirements on the leading jet p_T are set to ensure full trigger efficiency. However, Figure 5.4 reveals that the current signal selection is not taking advantage of the entire invariant mass regime for which the triggers are fully efficient. This indicates, that the single-jet triggers are capable of detecting dijet resonances with significantly lower invariant masses than currently achieved while maintaining full efficiency.

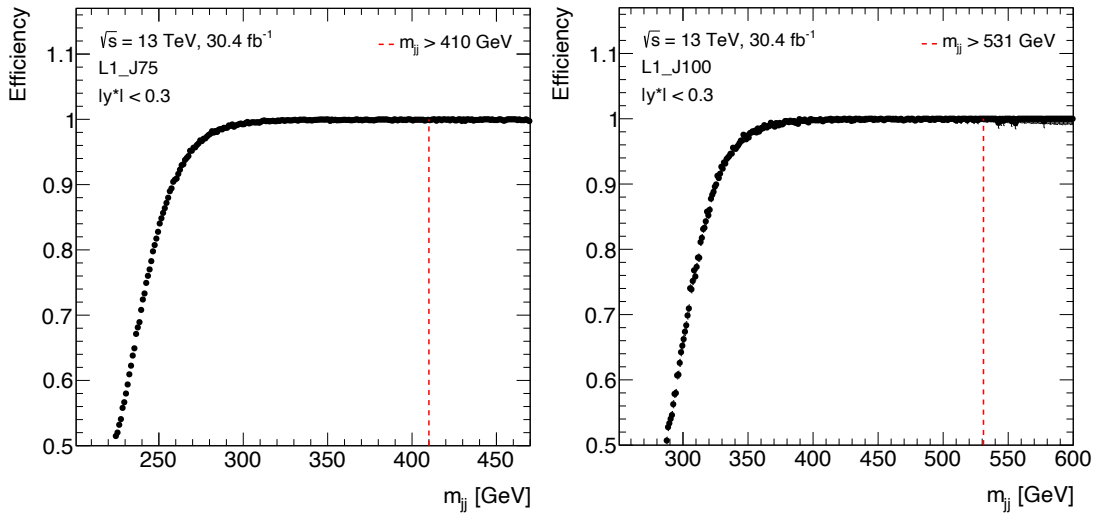

(a) J75 (b) J100

Figure 5.4: The turn-on curves for the respective Level-1 single-jet triggers used in the current signal selection approach as a function of m_{jj}. Level-1 J75 requires events to have $|y^*| < 0.3$, whereas J100 requires $|y^*| < 0.6$. The red lines depict the current lower boundary of the sensitivity region, hence no events below this threshold are considered.

The following section introduces an approach towards signal selection which makes use of the efficient phase space with respect to the dijet mass and thus extends the sensitivity to lower resonance masses. In addition, the potential of lower-p_T triggers, namely the L1 J50 and J40, is investigated in this context.

5.5 m_{jj}-based Signal Selection

In the current signal selection strategy, events are selected by cuts on the leading and subleading jet p_T. This significantly limits the exploitation of efficient phase space in terms of dijet mass.
I was shown on Monte-Carlo simulations that the introduction of a m_{jj} threshold rather than stringent p_T cuts on the respective jets allows to effectively make use

of the efficient phase space and significantly extend the sensitivity region to lower invariant masses [48]. This can be understood by considering that the current approach explicitly requires the leading jet to fire the trigger for the event to be recorded. Since the efficiency curves are not perfect step-functions, the efficiency for a given jet p_T is less than 100%. With the application of $|y^*|$ cuts, leading and subleading jet are of similar p_T values (see Section 5.2). Therefore it is possible that the subleading jet fires the trigger whereas the leading jet failed to. In this case, the event would be discarded if only p_T cuts are applied. In contrast, by only requiring an event to exceed an m_{jj} threshold, both the leading or subleading jet can fire the trigger and the event will be selected if it satisfies the requirement. For events with multiple jets, this indicates that an event has multiple chances to be selected by the trigger system. As a consequence, the leading jet p_T requirement can be lowered, resulting in significantly lower m_{jj} thresholds.
Furthermore, it was shown that the inclusion of lower-p_T single-jet triggers - here L1 J40 and J50 - allow to probe for even lower resonance masses following an m_{jj}-based selection strategy. Given that these results were obtained from MC simulations, the following sections will apply this approach on 2016 data to verify its implications. Furthermore, the optimal trigger selection criteria in terms of m_{jj}, jet-p_T and $|y^*|$ will be determined for the L1 single-jet triggers J100, J75, J50 and J40.

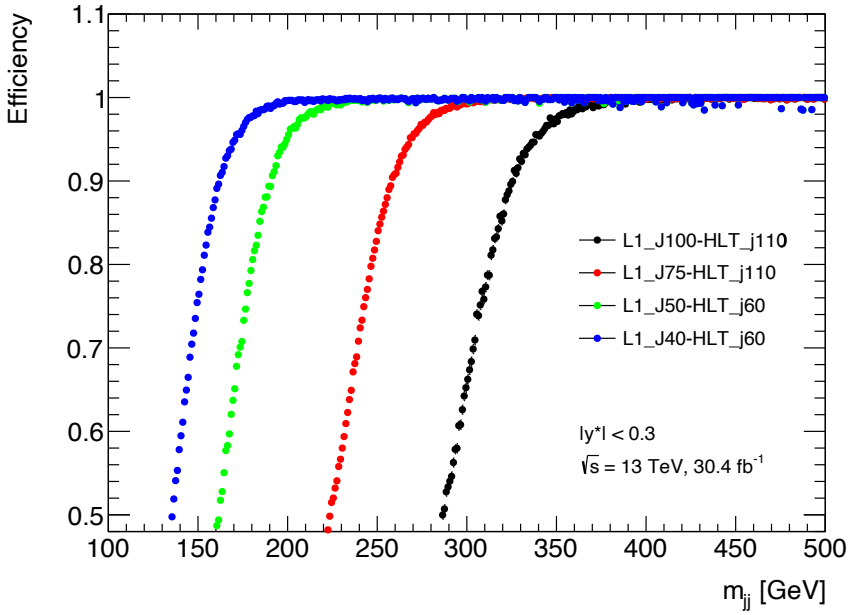

Figure 5.5: The turn-on curves for the L1 single-jet triggers J100, J75, J50 and J40 with respect to the reference HLT trigger-chains j110 and j60 as a function of m_{jj}. The events are required to satisfy $|y^*| < 0.3$.

5.5.1 m_{jj} Thresholds

In order to make full use of the efficient phase space of each trigger, the turn-on points of the respective efficiency curves are chosen as the trigger m_{jj} thresholds. The turn-on point denotes the invariant mass value for which the trigger exceeds an efficiency of 99.9%. The efficiency curves for the considered L1 triggers are shown in Figure 5.5 as a function of m_{jj} and with $|y^*| < 0.3$.

		m_{jj} thresholds [GeV]	
L1 Trigger	HLT Reference	$\|y^*\| < 0.3$	$\|y^*\| < 0.6$
J40	j60	227.6 ± 3.0	231.2 ± 4.1
J50	j60	246.6 ± 3.9	266.6 ± 3.8
J75	j110	326.7 ± 3.8	343.3 ± 2.7
J100	j110	413.2 ± 3.9	431.3 ± 3.3

Table 5.1: The m_{jj} values for which the respective L1 trigger exceeds an efficiency of 99.9% in the reference frame of the respective HLT trigger-chain. Results are shown for $|y^*| < 0.3$ and $|y^*| < 0.6$.

As discussed in Section 5.3, the m_{jj} threshold can be obtained by fitting a two-parametric sigmoid function to a reduced range of turn-on curves and determining the point where the trigger reaches an efficiency of 99.9% . The results are shown in Table 5.1. These were obtained from turn-on curves which additionally required p_T^{lead},$p_T^{sublead} > 85$ GeV. The helps to mitigate effects from pile-up interactions and is further discussed in Section 5.5.3.

	m_{jj}^* [GeV]	
L1 Trigger	$\|y^*\| < 0.3$	$\|y^*\| < 0.6$
J40	235	240
J50	260	280
J75	340	360
J100	425	445

Table 5.2: The fixed m_{jj} cuts for the respective L1 trigger signal selection. The cut is defined as the m_{jj} turn-on point plus two statistical deviations and then rounded up to the next 5 GeV bin. Results are shown for $|y^*| < 0.3$ and $|y^*| < 0.6$.

In order to derive fixed m_{jj} cuts from these results, the respective statistical errors were taken into account so that the fixed value m_{jj}^* is defined as the turn-on point plus two statistical deviations. To avoid bias from coarser binning, the cuts were rounded up to the lower edge of the next 5 GeV bin. The final cuts are shown

in Table 5.2. From there, it can be seen that the obtained m_{jj} thresholds for the L1 J75 and J100 are significantly lower than their current minimal detectable resonance masses. With the addition of lower-p_T single-jet triggers, m_{jj} thresholds as low as 235 GeV (J40) are possible.

5.5.2 Threshold-Dependency on HLT Reference Trigger

Given that L1 trigger efficiencies are determined with reference to an HLT trigger-chain, we need to ensure the obtained m_{jj} thresholds are not biased by the choice of the HLT reference frame.
As mentioned in Section 5.3, Level-1 jets are solely calibrated to the electromagnetic scale of the ATLAS calorimeters which does not necessarily reflect their true energy. This means that the visible jet energy for a L1 trigger does not take into account energy losses due to e.g. escaping particles in hadronic showers or uninstrumented detector material. In order to calibrate the jet energies to the Jet Energy Scale (JES) later on, correction factors, typically of order two, are applied to correct for the lost energy [47]. Therefore, the E_T thresholds of L1 triggers need to be interpreted in terms of the limited jet energy information. The HLT trigger-chains used as reference consist of an HLT trigger which is *seeded* by a low-p_T L1 trigger[1]. This allows for instance to use an HLT j110 trigger with a p_T > 110 GeV threshold as a reference for an L1 J100 with $E_T > 100$ GeV, since the former is scaled to the JES and the trigger chain is already fully efficient before L1 turn-on point.

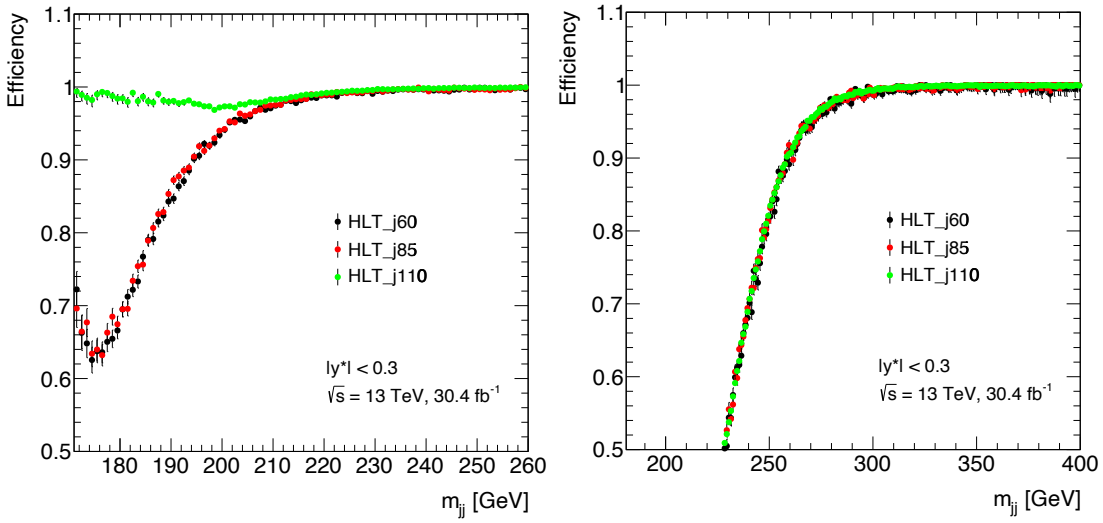

(a) J50 (b) J75

Figure 5.6: The efficiencies for the Level-1 single-jet triggers J50 and J75 for different reference HLT triggers. Events are required to have p_T^{lead},$p_T^{sublead} > 85$ GeV as well as $|y^*| < 0.3$.

[1]Detailed information on the assigned L1 triggers for HLT trigger seeding and the respective prescale factors can be found here [49].

Figure 5.6 shows the efficiencies of L1 J50 and L1 J75 for different HLT reference triggers as a function of m_{jj}. For both L1 triggers, the m_{jj} turn-on point seems to be unbiased from the choice of HLT reference trigger(see Figure 5.6a). This is confirmed by the results shown in Table 5.3.

	m_{jj} thresholds [GeV]		
L1	HLT j60	HLT j85	HLT j110
$\|y^*\| < 0.3$			
J40	227.6 ± 3.0	228.6 ± 6.0	-
J50	246.5 ± 3.9	244.9 ± 3.8	-
J75	336.6 ± 4.6	334.8 ± 5.3	326.7 ± 3.8
J100	-	427.9 ± 4.9	413.2 ± 3.9
$\|y^*\| < 0.6$			
J40	231.2 ± 4.1	232.8 ± 6.0	-
J50	266.6 ± 3.8	266.7 ± 2.5	-
J75	351.4 ± 3.8	346.9 ± 4.1	343.3 ± 2.7
J100	-	443.0 ± 4.0	431.3 ± 3.3

Table 5.3: The m_{jj} values for which the respective L1 single-jet trigger turns fully efficient with respect to the given HLT reference trigger. The results are given for $|y^*| < 0.3$ and $|y^*| < 0.6$.

Even though different HLT reference triggers do not yield the same m_{jj} thresholds, the values are still within reasonable range with respect to the statistical errors and do not differ more than one σ-deviation, except for the J100 with two σ-deviations.
In conclusion, the choice of HLT reference trigger does not pose a significant bias on the resulting m_{jj} thresholds of the respective L1 triggers. The selection given in Table 5.1 was made because these pairs yielded the most complete turn-on curves and lowest statistical errors on the fit results.

5.5.3 Jet-p_T Selection

In addition to an m_{jj} cut on the dijet selection, p_T requirements need to be posed on the leading and subleading jet in order to mitigate the effects of pile-up interactions. Whereas before, the leading jet p_T cut ensured that the trigger is running fully efficient, this is now guaranteed by requiring the event to exceed a certain invariant mass.
Figure 5.7 depicts the efficiency of the L1 single-jet triggers as a function of leading jet p_T. The events are selected according to the respective m_{jj} threshold of the trigger. The dotted lines demonstrate the p_T cut that would have been applied on the leading jet in a p_T-based signal selection. The cut values were obtained similarly to the m_{jj} thresholds from Table 5.1 by fitting equation (5.1) to the efficiency curves shown in Figure 5.3 for the respective L1 triggers and $|y^*|$ cuts.

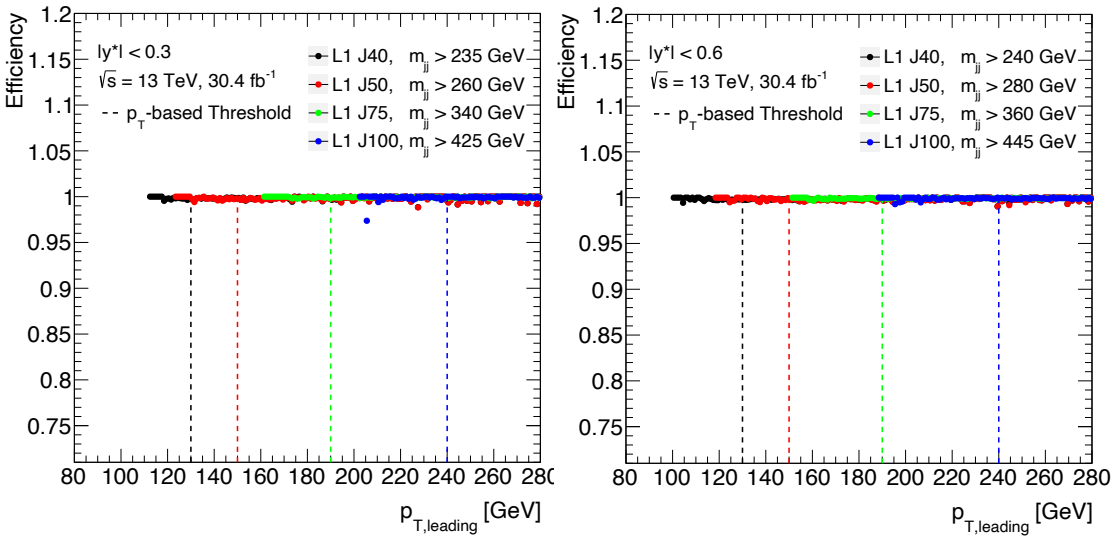

(a) $|y^*| < 0.3$ (b) $|y^*| < 0.6$

Figure 5.7: The efficiencies for the L1 single-jet triggers J100, J75, J50 and J40 as a function of the leading jet p_T. The events are selected by the trigger with reference to the m_{jj} thresholds from Table 5.2. The dotted lines depict the leading jet p_T threshold that would have been applied for a p_T-based signal selection approach. Results are shown for $|y^*| < 0.3$ and $|y^*| < 0.6$.

Both figures demonstrate that an m_{jj}-based signal selection extends the event acceptance to lower-p_T jets relative to a p_T-based efficiency approach while maintaining full trigger efficiency. In consequence, the requirements on the leading jet p_T can be considerably lowered.
With reference to Section 5.4, the current p_T requirement on the subleading jet is 85 GeV. A looser constraint on this dijet variable would mean that lower-p_T subleading jets could be selected by the trigger and therefore impair the signal sensitivity due to increased acceptance of pile-up interactions. As a compromise, both the leading and subleading p_T cuts could be placed at 85 GeV to avoid increased accumulation of pile-up signals in the trigger system but make full use of the efficient phase space.
In order to maintain flexibility for possible changes on the p_T cuts for the leading jet, it is necessary to determine the highest possible leading jet p_T threshold which accounts for no loss in statistics relative to a threshold of 85 GeV. If necessary, this allows for the cut to be chosen within these boundaries without making compromises on event statistics. The upper thresholds were determined by comparing the m_{jj} distributions of L1 single-jet triggers for different leading jet p_T cuts relative to $\mathrm{p_T^{lead}} > 85$ GeV. These cuts were applied to an HLT trigger that processes the selected events of L1, since the data requires a choice of HLT trigger due to differences in prescale factors. An example for the L1 J40 and J100 with the respective HLT triggers and applied m_{jj} cuts can be seen in Figure A.1.
The highest possible p_T threshold is chosen as the highest cut that yields a constant ratio of 1.0. The results for these upper boundaries on the choice of leading

jet p_T cut are shown in Table 5.4. From these, it can be deduced that the leading jet p_T selection thresholds can be considerably increased with no loss in the recorded event statistics.

	$p_T^{leading}$ [GeV]	
L1 Trigger	$\|y^*\| < 0.3$	$\|y^*\| < 0.6$
J40	110	100
J50	120	110
J75	160	150
J100	185	185

Table 5.4: The highest-possible p_T-cuts on the leading jet corresponding to no loss in statistics relative to $p_T^{leading} > 85$ GeV. Results are given for $|y^*| < 0.3$ and $|y^*| < 0.6$.

5.5.4 Dijet Selection in terms of $|y^*|$

As mentioned in Section 5.1, events are required to satisfy a certain $|y^*|$ threshold in order to pass the signal selection. Therefore, this section aims to investigate and optimize the choice of $|y^*|$ cut for the search of low resonance masses by incorporating the preceding results.

Dependency of m_{jj}-based Signal Selection on $|y^*|$

Section 5.2 was able to show that a $|y^*|$ cut on events with dijet final-states provokes that higher-p_T jets are selected for a given invariant mass, decreasing the difference of leading and subleading jet p_T.
This influence on the jet p_T-selection, however, also reflects in the obtained m_{jj} thresholds given in Table 5.1. From these results, it can be deduced that a more stringent choice of $|y^*|$ cut leads to lower m_{jj} thresholds for constant jet p_T selection criteria. This interpretation is validated by Figure 5.8a which depicts the efficiency of Level-1 trigger J100 as a function of the invariant dijet mass for different $|y^*|$ cuts applied. When comparing the efficiency curves for $|y^*| < 0.3$ and $|y^*| < 0.6$, one can see that the turn-on point of the L1 J100 is shifted to higher invariant masses for a looser cut. Given that subleading jets with higher transverse momenta are selected for stricter $|y^*|$ cuts, they possess an increased chance of satisfying the p_T requirement, resulting in lower turn-on points.
Another important conclusion that can be drawn from this figure is that an m_{jj}-based signal selection approach for the J100 explicitly requires an additional $|y^*|$ cut on dijet events in order to guarantee that the trigger is running at full efficiency. This is due to the fact that with no cut applied, the L1 J100 trigger does not turn fully efficient. This can be understood from considering that with no $|y^*|$ cut applied on the events, the trigger signal input for a given invariant dijet mass is dominated by low-p_T jets. Since jets of low transverse momenta are captured

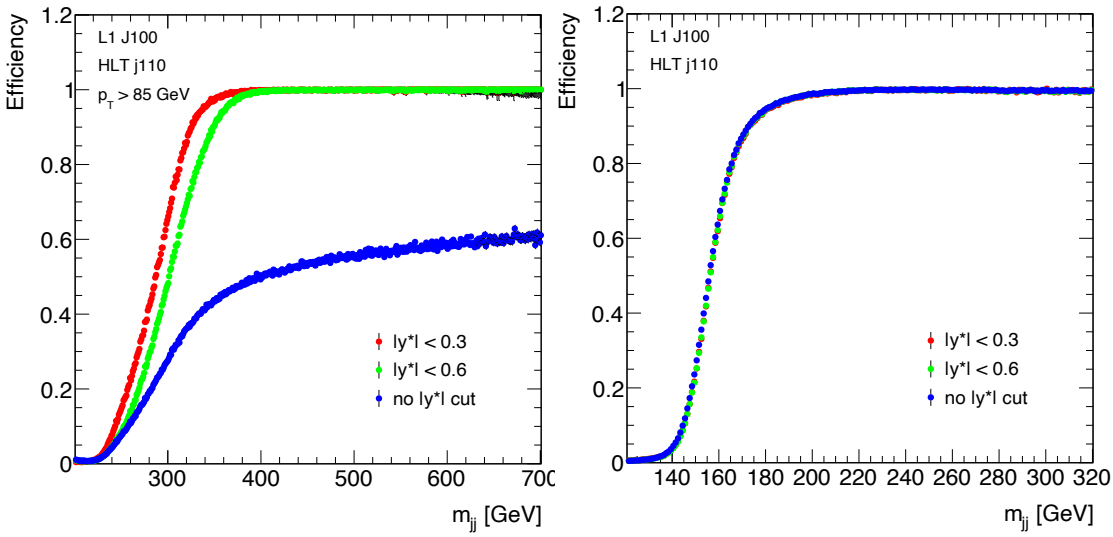

(a) (b)

Figure 5.8: The efficiencies for the Level-1 single-jet trigger J100 for $|y^*| < 0.3$, $|y^*| < 0.6$ and no $|y^*|$-cut. Figure 5.8a shows the efficiency as a function of m_{jj} and furthermore requires the leading jet $p_T > 85$ GeV, whereas 5.8b depicts the efficiency as a function of leading jet-p_T.

with trigger efficiencies smaller than 100% (see Figure 5.3), the trigger does not turn fully efficient with respect to m_{jj} for sub-TeV masses. In contrast, Figure 5.8b shows that the turn-on point of the J100 with respect to the leading jet p_T is unbiased from the choice of $|y^*|$ cut. This demonstrates that the leading jet p_T thresholds used in the preliminary signal selection approach did not need to be adjusted to the choice of $|y^*|$ cut. The same results were obtained for the other L1 single-jet triggers J40, J50 and J75.
In conclusion, this means that opposed to the previously used p_T-based selection approach, the m_{jj}-based signal selection specifically requires a $|y^*|$ cut on the selected events for the triggers to run fully efficient. In addition, the applied m_{jj} thresholds to each respective L1 trigger need to be adjusted to the choice of $|y^*|$ requirement.

Signal-Sensitivity in Dependence of $|y^*|$

Since this emphasizes the importance of a $|y^*|$ cut in an m_{jj}-based signal selection strategy, this section aims to optimize this criterion so that the m_{jj} threshold can be adjusted accordingly. A very important measure for the goodness of the trigger selection with respect to the search for low-mass resonances is the signal-to-background ratio. It describes the ratio of the mass resonance bump relative to the background signal to compare the signal sensitivity for different selection criteria.
In order to investigate the dependence of the signal-to-background ratio on the choice of $|y^*|$ cut, Monte-Carlo (MC) simulations for different signal samples were

taken. The simulations reflect possible resonances for different mediator masses $m_{Z'}$ and Standard Model coupling constants g_{SM}. These were generated using MadGraph 5 (v.2.2.3), PYTHIA8 (v.8.21) and EvtGen(v.1.2.0).[2]

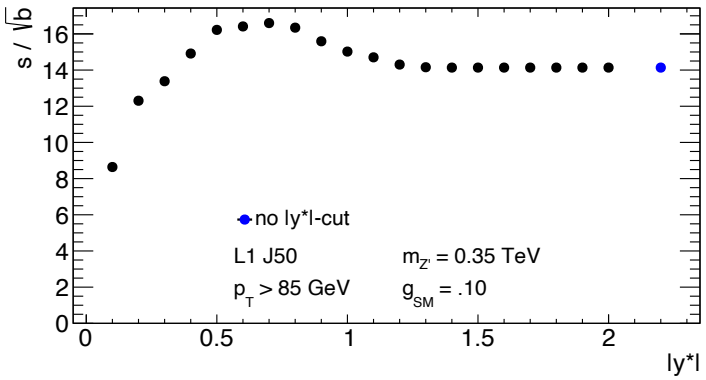

(a)

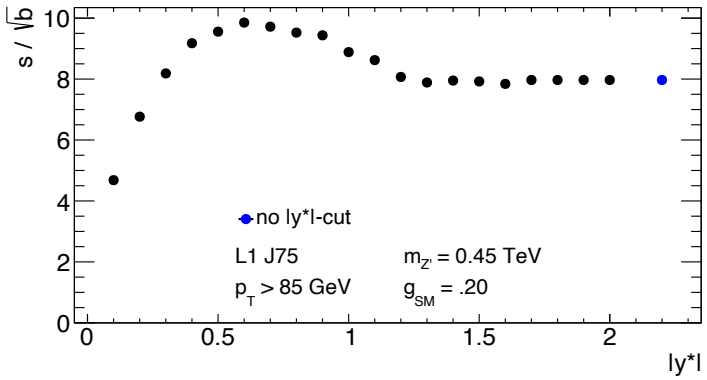

(b)

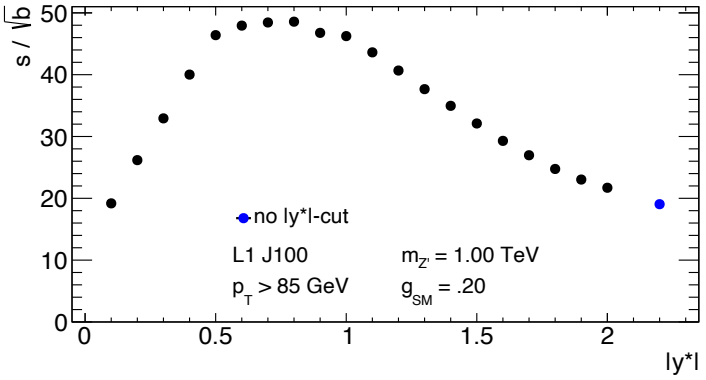

(c)

Figure 5.9: The signal-to-background ratio as a function of the $|y^*|$ cut for different resonance masses $m_{Z'}$ and coupling constants g_{SM}. The event selection was carried out with respect to the L1 trigger that covers the mass regime in which the resonance mass lies. Events are required to have p_T^{lead}, $p_T^{sublead} > 85$ GeV.

[2]More information on event generation using Monte-Carlo simulations can be found here [50]. Detailed information on the respective generators are further given in [51–53].

To determine the signal-to-background ratio, a Gaussian function was fitted to the right side of the resonance peak to obtain its standard deviation σ. Only the right side was used since the signal distribution can be described by a Crystal Ball function, where a Gaussian transitions into an exponential function above a defined threshold. Figures A.2a to A.2c show that the right side of the signal peak follows a Gaussian distribution. The ratio was then obtained by integrating the signal and background distribution within one σ-deviation of the peak respectively and dividing the signal counts by the square-root of the background counts. In this analysis, three different signal samples were used, corresponding to resonance masses of a Z' mediator particle of 350 GeV, 450 GeV and 1 TeV. The signal-sensitivity of the samples for different $|y^*|$ cuts was examined with respect to the Level-1 trigger that covers the respective mass region, meaning that the trigger is fully efficient for the resonance mass but the next higher L1 trigger is not. The optimal $|y^*|$ cut for the specific trigger would then yield the largest signal-to-background ratio. The results are shown in Figures 5.9a to 5.9c.
From the three figures it can be observed that for resonance masses of 1 TeV and 350 GeV, a $|y^*| < 0.7$ requirement yields the highest signal sensitivity, whereas $|y^*| < 0.6$ is optimal for $m_{Z'} = 450$ GeV. Given that the difference of these maxima equals the bin width, it can be generally concluded that a requirement of $|y^*| < 0.6$ is sufficient to guarantee an optimal sensitivity to Z'-resonances in the sub-TeV mass-range. This applies to the Level-1 triggers J50, J75 and J100, but should not deviate considerably for the J40.

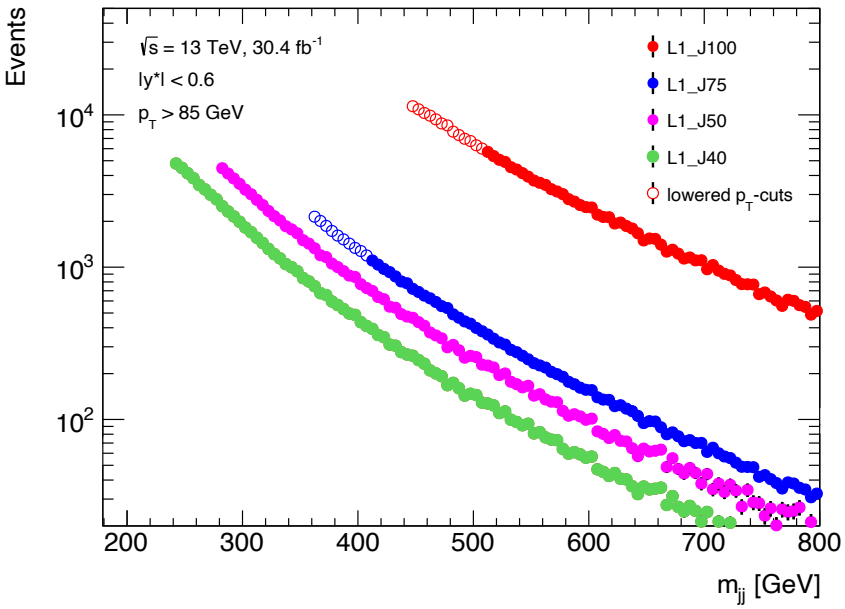

Figure 5.10: The distribution of invariant dijet mass for the Level-1 single-jet triggers J100, J75, J50 and J40. In terms of signal selection, the applied m_{jj} thresholds are set at 445 GeV, 360 GeV, 280 GeV and 240 GeV, respectively. Further, events are required to satisfy $|y^*| < 0.6$ as well as $p_T > 85$ GeV for the two highest-momenta jets.

The reason for why looser $|y^*|$ constraints yield a decreased signal sensitivity can be found in the fact that the turn-on points of the L1 triggers are shifted to higher invariant masses for looser cuts, as discussed above. Henceforth, the trigger does not select sub-TeV dijet events at full efficiency for higher cuts.
For an optimal signal selection, the applied m_{jj} cuts need to be chosen with respect to a $|y^*| > 0.6$ cut, whereas the additional p_T cuts are independent of this selection variable. Figure 5.10 shows the resulting invariant dijet mass distributions for the L1 triggers with the determined thresholds applied. For the L1 J75 and J100 it is further illustrated how lower p_T requirements have allowed to extend the sensitivity region to lower invariant masses.

Chapter 6

Conclusion

An analysis for improving the signal selection criteria for a variety of Level-1 (L1) single-jet triggers was carried out with regard to a trigger-level dijet search. In order to extend the search to lower resonance masses, the selection thresholds on m_{jj}, p_T and $|y^*|$ for dijet events were optimized for the respective L1 triggers. These include previously used triggers - J100 and J75 - as well as new lower-p_T triggers - J50 and J40.
Following an m_{jj}-based efficiency approach, the trigger event selection was defined such that only events with an invariant mass above the 99.9% efficiency point of the respective trigger are selected. It was shown that this allows to considerably lower the requirements on the leading jet p_T. In consequence, the L1 J100 and J75 triggers are able to extend the respective sensitivity regions of the trigger-level analysis by about 100 GeV relative to the current signal selection. In addition, the L1 J40 and J50 have proven that they allow to probe for resonance masses as low as 235 GeV while maintaining full trigger efficiency. Given that a $|y^*|$ requirement is crucial for this selection approach, the respective threshold was optimized with regard to an optimal signal sensitivity for sub-TeV resonance masses.
The significance of the presented results reflects in the fact that the optimized signal selection as well as the low threshold triggers allow to extend the search for low mass mediators in dijet signatures to substantially lower masses. Considering that these results were obtained using data collected in 2016, a useful extension would be to carry out the analysis on 2017 and 2018 data since they offer different pile-up profiles as well as different beam configurations that affect the L1 configuration and jet reconstruction procedures.

Appendix A

Additional Plots

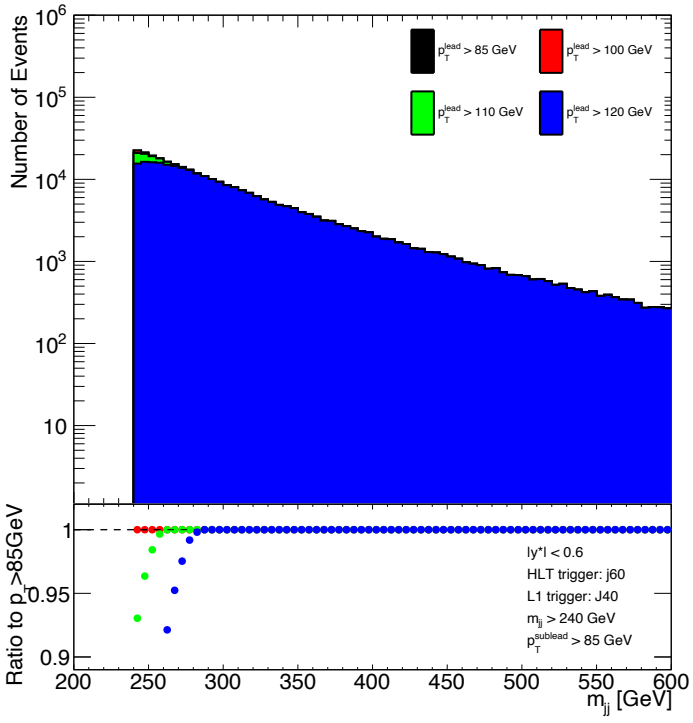

(a)

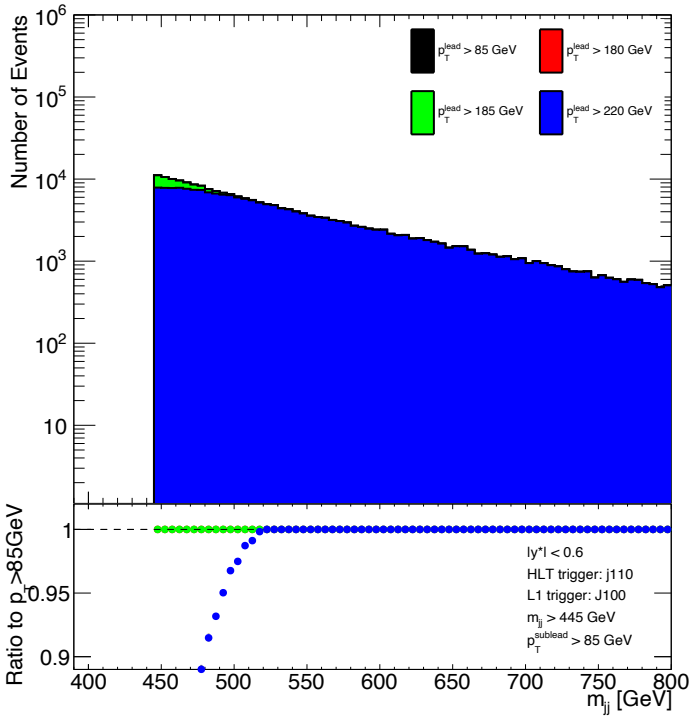

(b)

Figure A.1: The m_{jj} distribution of HLT triggers j60 and j110 for different leading jet p_T-cuts as well as the ratio relative to $p_T^{lead} > 85$ GeV. Events are required to have $|y^*| < 0.6$ and $p_T^{sublead} > 85$ GeV. The j60 further requires $m_{jj} > 240$ GeV, whereas the j110 requires $m_{jj} > 445$ GeV.

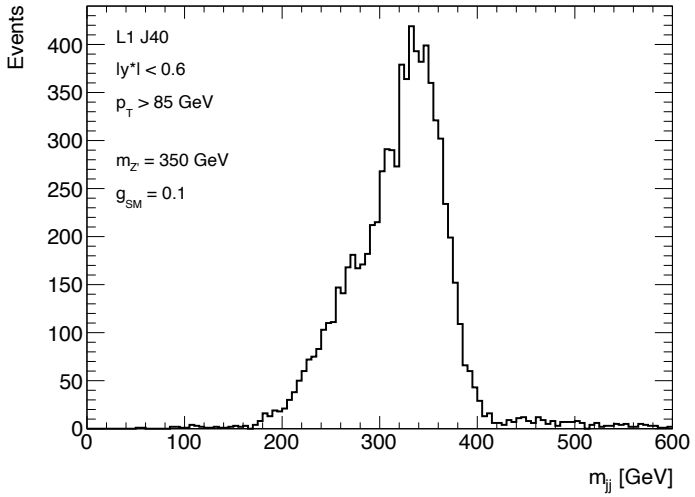

(a)

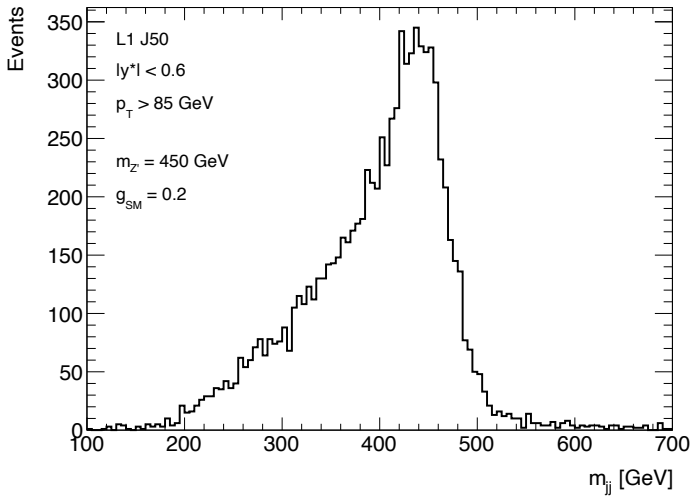

(b)

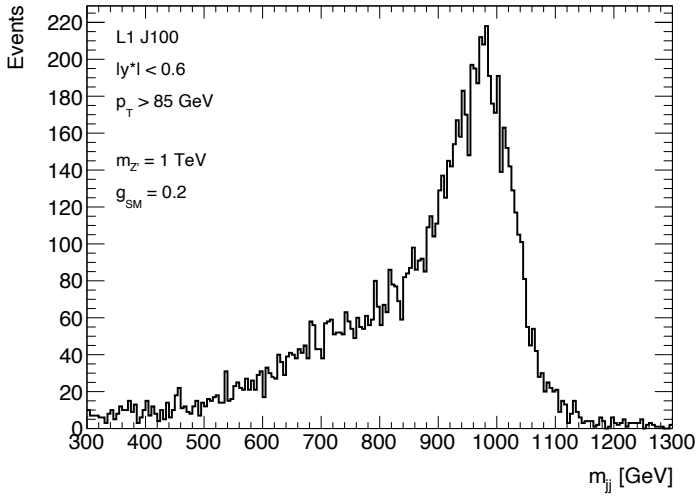

(c)

Figure A.2: Monte-Carlo simulations for Z' mediator resonance signals for different particle masses $m_{Z'}$ and coupling constants g_{SM}. Signals are selected by the efficient trigger in the respective mass region. Events further need to satisfy $p_T > 85$ GeV and $|y^*| < 0.6$ to be considered.

Bibliography

[1] Fritz Zwicky. "Die Rotverschiebung von extragalaktischen Nebeln". In: *Helvetica physica acta* 6 (1933).

[2] Marcela Carena et al. "MSSM Higgs boson searches at the LHC: benchmark scenarios after the discovery of a Higgs-like particle". In: *The European Physical Journal C* 73 (2013).

[3] K Kodama et al. "Observation of tau neutrino interactions". In: *Physics Letters B* 504.3 (2001).

[4] Claudio Campagnari and Melissa Franklin. "The discovery of the top quark". In: *Rev. Mod. Phys.* 69 (1 Jan. 1997). DOI: 10.1103/RevModPhys.69.137.

[5] Matts Roos. *Dark Matter: The evidence from astronomy, astrophysics and cosmology*. 2010. arXiv: 1001.0316 [astro-ph.CO].

[6] Antonio Boveia and Caterina Doglioni. "Dark Matter Searches at Colliders". In: *Annual Review of Nuclear and Particle Science* 68.1 (Oct. 2018). ISSN: 1545-4134. DOI: 10.1146/annurev-nucl-101917-021008. URL: http://dx.doi.org/10.1146/annurev-nucl-101917-021008.

[7] The ATLAS Collaboration. "Search for new phenomena in dijet events using 37 fb−1 of pp collision data collected at $\sqrt{s}$=13 TeV with the ATLAS detector". In: *Physical Review D* 96.5 (Sept. 2017). ISSN: 2470-0029. DOI: 10.1103/physrevd.96.052004. URL: http://dx.doi.org/10.1103/PhysRevD.96.052004.

[8] The ATLAS Collaboration. "Search for low-mass dijet resonances using trigger-level jets with the ATLAS detector in pp collisions at sqrt(s)=13 TeV". In: *Phys. Rev. Lett.* 121 (2018). DOI: 10.1103/PhysRevLett.121.081801. URL: https://arxiv.org/abs/1804.03496.

[9] *UKRI Science and Technology Facilities Council*. https://stfc.ukri.org/research/particle-physics-and-particle-astrophysics/peter-higgs-a-truly-british-scientist/why-is-the-higgs-discovery-so-significant/. [Accessed: 2021-02-03].

[10] W. Pauli. "The Connection Between Spin and Statistics". In: *Phys. Rev.* 58 (8 Oct. 1940). DOI: 10.1103/PhysRev.58.716. URL: https://link.aps.org/doi/10.1103/PhysRev.58.716.

[11] Yoshiyuki Fukuda et al. "Evidence for oscillation of atmospheric neutrinos". In: *Physical Review Letters* 81.8 (1998).

[12] S. F. King. "Neutrino mass models". In: *Reports on Progress in Physics* 67 (Dec. 2003). DOI: 10.1088/0034-4885/67/2/r01. URL: https://doi.org/10.1088/0034-4885/67/2/r01.

[13] W.N. Cottingham and D.A. Greenwood. *An Introduction to the Standard Model of Particle Physics*. Cambridge University Press, 2007. ISBN: 9781139462211. URL: https://books.google.de/books?id=Dm36BYq9iu0C.

[14] Robert M. Harris and Konstantinos Kousouris. "Searches for Dijet Resonances at Hadron Colliders". In: *International Journal of Modern Physics A* 26 (Dec. 2011). ISSN: 1793-656X. DOI: 10.1142/s0217751x11054905. URL: http://dx.doi.org/10.1142/S0217751X11054905.

[15] Lydia Audrey Beresford. "Searches for dijet resonances using $\sqrt{s} = 13$ TeV proton-proton collision data recorded by the ATLAS detector at the Large Hadron Collider". PhD thesis. University of Oxford, 2017.

[16] Simone Marzani, Gregory Soyez, and Michael Spannowsky. *Looking inside jets: an introduction to jet substructure and boosted-object phenomenology*. Springer, 2019.

[17] Mark Thomson. *Modern particle physics*. Cambridge University Press, 2013.

[18] The University of New South Wales. *The Planck scale: relativity meets quantum mechanics meets gravity*. https://newt.phys.unsw.edu.au/einsteinlight/jw/module6_Planck.html. [Accessed: 2021-02-12].

[19] Raymond Davis. "A review of the Homestake solar neutrino experiment". In: *Progress in Particle and Nuclear Physics* 32 (1994). ISSN: 0146-6410. DOI: https://doi.org/10.1016/0146-6410(94)90004-3. URL: https://www.sciencedirect.com/science/article/pii/0146641094900043.

[20] Vera C Rubin, W Kent Ford Jr, and Norbert Thonnard. "Rotational properties of 21 SC galaxies with a large range of luminosities and radii, from NGC 4605/R= 4kpc/to UGC 2885/R= 122 kpc". In: *The Astrophysical Journal* 238 (1980).

[21] Sinclair Smith. "The Mass of the Virgo Cluster". In: *Astrophys. J.* 83 (1936). DOI: 10.1086/143697.

[22] Richard Massey, Thomas Kitching, and Johan Richard. "The dark matter of gravitational lensing". In: *Reports on Progress in Physics* 73 (2010).

[23] Carlos S Frenk and Simon DM White. "Dark matter and cosmic structure". In: *Annalen der Physik* 524 (2012).

[24] Alexey Boyarsky, Oleg Ruchayskiy, and Mikhail Shaposhnikov. "The role of sterile neutrinos in cosmology and astrophysics". In: *Annual Review of Nuclear and Particle Science* 59 (2009).

[25] *Neutrinos as Dark Matter*. http://www.astro.ucla.edu/~wright/neutrinos.html. [Accessed: 2021-02-08].

[26] Manoj Kaplinghat, Lloyd Knox, and Yong-Seon Song. "Determining Neutrino Mass from the Cosmic Microwave Background Alone". In: *Phys. Rev. Lett.* 91 (Dec. 2003). DOI: 10.1103/PhysRevLett.91.241301. URL: https://link.aps.org/doi/10.1103/PhysRevLett.91.241301.

[27] Gianfranco Bertone, Dan Hooper, and Joseph Silk. "Particle dark matter: evidence, candidates and constraints". In: *Physics Reports* 405 (Jan. 2005). ISSN: 0370-1573. DOI: 10.1016/j.physrep.2004.08.031. URL: http://dx.doi.org/10.1016/j.physrep.2004.08.031.

[28] Graciela B Gelmini. "The hunt for dark matter". In: *Journeys Through the Precision Frontier: Amplitudes for Colliders: TASI 2014 Proceedings of the 2014 Theoretical Advanced Study Institute in Elementary Particle Physics*. World Scientific, 2016.

[29] Morad Aaboud et al. "Constraints on mediator-based dark matter and scalar dark energy model using $\sqrt{s}$= 13 TeV p collision data collected by the ATLAS detector". In: *Journal of High Energy Physics* 2019 (2019).

[30] Oliver Sim Brüning et al. *LHC Design Report*. CERN Yellow Reports: Monographs. Geneva: CERN, 2004. DOI: 10.5170/CERN-2004-003-V-1. URL: https://cds.cern.ch/record/782076.

[31] The ATLAS Collaboration. "The ATLAS Experiment at the CERN Large Hadron Collider". In: *Journal of Instrumentation* 3.08 (Aug. 2008). DOI: 10.1088/1748-0221/3/08/s08003. URL: https://doi.org/10.1088/1748-0221/3/08/s08003.

[32] *The ATLAS muon system*. https://cds.cern.ch/record/2197559. [Accessed: 2021-02-16].

[33] Hanno Meyer zu Theenhausen. "Search for Light Dijet Resonances using Trigger Jets with the ATLAS Experiment at the Large Hadron Collider". PhD thesis. Universität Heidelberg, 2018.

[34] Joao Pequenao. "Computer generated image of the whole ATLAS detector". Mar. 2008. URL: https://cds.cern.ch/record/1095924.

[35] The ATLAS Collaboration. *ATLAS inner detector: Technical Design Report 1*. Technical design report. ATLAS. Geneva: CERN, 1997. URL: https://cds.cern.ch/record/331063.

[36] *The CERN accelerator complex*. https://www.mpp.mpg.de/en/research/structure-of-matter/atlas-detector-particle-collisions-at-the-lhc/atlas-muon-spectrometer. [Accessed: 2021-03-19].

[37] Aranzazu Ruiz-Martinez and ATLAS Collaboration. *The Run-2 ATLAS Trigger System*. Tech. rep. ATL-DAQ-PROC-2016-003. Accessed: 2021-02-20. Geneva: CERN, Feb. 2016. DOI: 10.1088/1742-6596/762/1/012003. URL: https://cds.cern.ch/record/2133909.

[38] "Performance of the ATLAS Trigger System in 2015". In: *Eur. Phys. J. C* 77.CERN-EP-2016-241. 5 (Nov. 2016). DOI: 10.1140/epjc/s10052-017-4852-3. URL: https://cds.cern.ch/record/2235584.

[39] Claire Antel. "Enhancing low mass dark matter mediator resonance searches with improved triggering in the ATLAS detector". PhD thesis. Universität Heidelberg, 2019.

[40] Imma Riu and on behalf of the ATLAS Collaboration. "The ATLAS Level-1 Topological Trigger performance in Run 2". In: *Journal of Physics: Conference Series* 898 (Oct. 2017). DOI: 10.1088/1742-6596/898/3/032037. URL: https://doi.org/10.1088/1742-6596/898/3/032037.

[41] The ATLAS Collaboration. *Dark Matter Summary Plots*. [Accessed 26.03.2021]. 2020. URL: https://atlas.web.cern.ch/Atlas/GROUPS/PHYSICS/PUBNOTES/ATL-PHYS-PUB-2020-021/.

[42] The ATLAS Collaboration. "Search for light dijet resonances with the ATLAS detector using a Trigger-Level Analysis in LHC pp collisions at $\sqrt{s} = 13$ TeV". In: (June 2016).

[43] The ATLAS Collaboration. *Trigger-object Level Analysis with the ATLAS detector at the Large Hadron Collider: summary and perspectives*. Tech. rep. ATL-DAQ-PUB-2017-003. Geneva: CERN, Dec. 2017. URL: https://cds.cern.ch/record/2295739.

[44] Antonio Boveia Caterina Dogloni. *Trigger Level Analyses in ATLAS*. [Accessed 04.03.2021]. 2017. URL: https://indico.cern.ch/event/606421/contributions/2558028/attachments/1445860/2227281/20170418_boveia_lbl.pdf.

[45] The ATLAS Collaboration. *Trigger Operation Public Results*. [Accessed 06.03.2021]. URL: https://twiki.cern.ch/twiki/bin/view/AtlasPublic/Trigger-OperationPublicResults.

[46] Matteo Cacciari, Gavin P Salam, and Gregory Soyez. "The anti-ktjet clustering algorithm". In: *Journal of High Energy Physics* 2008.04 (Apr. 2008). ISSN: 1029-8479. DOI: 10.1088/1126-6708/2008/04/063. URL: http://dx.doi.org/10.1088/1126-6708/2008/04/063.

[47] Steven Schramm. *ATLAS Jet Reconstruction, Calibration, and Tagging of Lorentz-boosted Objects*. Tech. rep. ATL-PHYS-PROC-2017-236. Geneva: CERN, Nov. 2017. URL: https://cds.cern.ch/record/2291608.

[48] Elena van der Vorst. "Optimisation of Signal Selection in a Search for Low Mass Mediators in Dijet Signatures". Bachelor's Thesis. Imperial College London, July 2020.

[49] David Miller. *ATLAS Trigger Software: Jet Trigger Menu*. [Accessed 12.03.2021]. 2016. URL: https://its.cern.ch/jira/browse/ATR-9521.

[50] Michael H. Seymour and Marilyn Marx. *Monte Carlo Event Generators*. Lecture. 2013. arXiv: 1304.6677 [hep-ph].

[51] Johan Alwall et al. "MadGraph 5: going beyond". In: *Journal of High Energy Physics* 2011.6 (2011).

[52] Torbjörn Sjöstrand et al. “An introduction to PYTHIA 8.2”. In: *Computer Physics Communications* 191 (June 2015). ISSN: 0010-4655. DOI: 10.1016/j.cpc.2015.01.024. URL: http://dx.doi.org/10.1016/j.cpc.2015.01.024.

[53] David J. Lange. “The EvtGen particle decay simulation package”. In: *Nuclear Instruments and Methods in Physics Research Section A: Accelerators, Spectrometers, Detectors and Associated Equipment* 462.1 (2001). DOI: https://doi.org/10.1016/S0168-9002(01)00089-4.

Acknowledgements

At the very end of my thesis, I would like to thank all the people that supported me throughout this process and made it so much more enjoyable.
I would like to express my very great appreciation to my supervisor Dr. Monica Dunford for giving me the opportunity to work in such a wonderful research group. I would also like to extend my special thanks to Falk for answering my endless questions and teaching me so much. It was a pleasure to partake in our weekly meetings and I would like to express my gratitude to both of you for your help and guidance.
I want to thank everyone in the ATLAS group at the KIP institute for your warm welcome and helpfulness. I also wish to express my gratitude to everyone who took the time to proofread parts of my thesis: Tigran, Sebastian, Martin, Falk and Lukas.
Lastly, I would like to thank my parents and my grandparents for their endless love and support throughout my studies.

Erklärung

Ich versichere, dass ich diese Arbeit selbstständig verfasst und keine anderen als die angegebenen Quellen und Hilfsmittel benutzt habe.

Heidelberg, den 02.04.2021 .....